UNIVERSIDAD DE INVESTIGACIÓN DE TECNOLOGÍA EXPERIMENTAL YACHAY

Escuela de Ciencias Físicas y Nanotecnología

TÍTULO: A view of shocks and time-scales in galactic wind-cloud models

Trabajo de integración curricular presentado como requisito para la obtención del título de Físico

Autor:

Pinargote Morrillo Bryan Joel

Tutor:

Ph.D Banda-Barragán Wladimir E.

Urcuquí, noviembre 2024

AUTORÍA

Yo, **Pinargote Morrillo Bryan Joel**, con cédula de identidad 1311629214, declaro que las ideas, juicios, valoraciones, interpretaciones, consultas bibliográficas, definiciones y conceptualizaciones expuestas en el presente trabajo; así cómo, los procedimientos y herramientas utilizadas en la investigación, son de absoluta responsabilidad de el/la autora (a) del trabajo de integración curricular. Así mismo, me acojo a los reglamentos internos de la Universidad de Investigación de Tecnología Experimental Yachay.

Urcuquí, noviembre 2024.

Firmado electrónicamente por:
BRYAN JOEL
PINARGOTE MORRILLO

Bryan Joel Pinargote Morrillo
CI: 1311629214

AUTORIZACIÓN DE PUBLICACIÓN

Yo, **Pinargote Morrillo Bryan Joel,** con cédula de identidad 1311629214, cedo a la Universidad de Investigación de Tecnología Experimental Yachay, los derechos de publicación de la presente obra, sin que deba haber un reconocimiento económico por este concepto. Declaro además que el texto del presente trabajo de titulación no podrá ser cedido a ninguna empresa editorial para su publicación u otros fines, sin contar previamente con la autorización escrita de la Universidad.

Asimismo, autorizo a la Universidad que realice la digitalización y publicación de este trabajo de integración curricular en el repositorio virtual, de conformidad a lo dispuesto en el Art. 144 de la Ley Orgánica de Educación Superior

Urcuquí, noviembre 2024.

Firmado electrónicamente por:
BRYAN JOEL
PINARGOTE MORRILLO

Bryan Joel Pinargote Morrillo
CI: 1311629214

DEDICATORIA

Para mis padres, hermanos, novia, amigos y compañeros.

Bryan Pinargote

ACKNOWLEDGEMENTS

The author of this thesis gratefully acknowledges the Gauss Centre for Supercomputing e.V. (www.gauss-centre.eu) for funding this project by providing computing time (via grant pn34qu) on the GCS Supercomputer SuperMUC-NG at the Leibniz Supercomputing Centre (www.lrz.de). The author of this thesis also acknowledges using the PLUTO code for performing the numerical simulations, the Python library Matplotlib and VisIt for scientific visualisation, and Google's AI Gemini for improving grammar and spelling errors in selected parts of the text.

Bryan Pinargote

RESUMEN

Los modelos de viento-nube han sido esenciales para comprender los procesos a pequeña escala que ocurren en los vientos galácticos. Durante estas interacciones se generan ondas de choque. Algunas ondas de choque emergen en el medio ambiente y otras son internas a la nube. Los choques internos pueden comprimir el gas en escalas de tiempo del orden del llamado tiempo de aplastamiento de la nube. Esta escala de tiempo indica cuánto tarda la onda de choque en atravesar la nube y se utiliza para normalizar los tiempos de simulación. La definición matemática de esta cantidad se basa en consideraciones analíticas de las presiones involucradas en la interacción viento-nube, pero a menudo difiere de las escalas de tiempo calculadas numéricamente. Esto ocurre particularmente cuando se consideran geometrías de nubes no uniformes o fractales. Esta tesis investiga el impacto del tamaño de la nube y la distribución inicial de densidad en los sistemas viento-nube, las estructuras de choque y las escalas de tiempo de disrupción de la nube utilizando simulaciones hidrodinámicas 3D y un novedoso algoritmo de seguimiento de choques. Consideramos nubes con diferentes tamaños y distribuciones de densidad con bordes agudos y suaves. Usando nuestra nueva rutina de detección de choques, pudimos rastrear efectivamente las células de choque internas y la célula de nube densa más alejada. Nuestros resultados confirman que la ecuación de Jones proporciona una mejor aproximación en comparación con la aproximación de Klein, con una diferencia de solo 0.33% respecto a las simulaciones numéricas para nubes completamente esféricas. Sin embargo, para nubes con una distribución de densidad no uniforme, como nubes con bordes suaves, esta aproximación analítica no se ajusta adecuadamente, con diferencias del 30.9%. Por lo tanto, proporcionamos una versión modificada de la ecuación de Jones, que tiene en cuenta la densidad promedio volumétrica media de la nube y proporciona una mejor aproximación al resultado obtenido numéricamente, con una diferencia de solo 4.59%. En general, nuestro estudio ayuda a comprender las interacciones viento-nube y proporciona un marco numérico para rastrear choques y calcular el tiempo de aplastamiento de la nube, que puede adaptarse a otras geometrías de nube.

Palabras Clave:

Medio interestelar, hidrodinámica, tiempo de aplastamiento de la nube, computación de alto rendimiento, simulaciones, número de Mach.

ABSTRACT

Wind-cloud models have been essential in understanding the small-scale processes occurring in galactic winds. Shocks are generated during such interactions. Some shock waves emerge in the ambient medium and some are internal to the cloud. The internal shocks can compress the gas on time-scales of the order of the so-called cloud-crushing time. This time-scale indicates how long it takes for the shock to travel across the cloud and is used to normalize the simulation times. The mathematical definition of this quantity is based on analytical considerations of the pressures involved in the wind-cloud interaction, but it often differs from the numerically-calculated time-scales. This happens particularly when non-uniform or fractal cloud geometries are considered. This thesis investigates the impact of cloud size and initial density distribution on wind-cloud systems, shock structures, and cloud disruption time-scales using 3D hydrodynamic simulations and a novel shock-tracking algorithm. We considered clouds with different sizes and density distributions with sharp and smooth edges. Using our new shock-finding routine, we were able to effectively track the internal shock cells and the most downstream dense cloud cell. Our results confirm that the Jones equation provides a better approximation compared to the Klein approximation, with a difference of only 0.33% from numerical simulations for completely spherical clouds. However, for clouds with a non-uniform density distribution, such as clouds with smooth edges, this analytical approximation does not fit properly with differences of 30.9%. Therefore, we provide a modified version of the Jones equation, which takes into account the cloud mean volume-average density and provides a better approximation to the numerically-obtained result, with a difference of only 4.59%. Overall, our study helps to understand wind-cloud interactions and provides a numerical framework to track shocks and calculate the cloud-crushing time, which can be further adapted to other cloud geometries.

Key Words:

Interstellar medium, hydrodynamics, cloud-crushing time, high performance computing, simulations, Mach number.

Contents

List of Figures **viii**

List of Tables **xi**

List of Papers **xiii**

1 Introduction **1**
- 1.1 Structure of spiral galaxies . . . 1
- 1.2 Wind-cloud systems in the ISM . . . 3
- 1.3 Problem Statement . . . 4
- 1.4 General and Specific Objectives . . . 5

2 Methodology **7**
- 2.1 Numerical setup of the PLUTO code: . . . 7
- 2.2 Post-processing (data analysis and visualization) tools: . . . 9
  - 2.2.1 I/O python functions: . . . 10
  - 2.2.2 Our Shock Finder Python module: . . . 11
  - 2.2.3 Shock tracking routine for the internal cloud shock: . . . 12
- 2.3 Computational Requirements . . . 12
- 2.4 Simulation setup and models . . . 13
  - 2.4.1 Initial conditions . . . 13
  - 2.4.2 Boundary conditions . . . 15
- 2.5 Diagnostics . . . 15
  - 2.5.1 Cloud geometry . . . 16
  - 2.5.2 Cloud dynamics . . . 16
  - 2.5.3 Turbulence parameters . . . 16

3 Results & Discussion **19**
- 3.1 Evolution of wind-cloud systems . . . 19

3.2 The role of cloud morphology 22
3.3 Shocks in wind-cloud models 27
  3.3.1 Searching for convergent flows: 27
  3.3.2 Searching for large pressure gradients: 27
  3.3.3 Shock population and typical shock Mach numbers: 30
  3.3.4 Histograms of shock Mach numbers: 30
3.4 On cloud-crushing times from the internal shock viewpoint 33
  3.4.1 Analytical approach 33
  3.4.2 Numerical approach 34
  3.4.3 Redefining the calculation of the cloud-crushing time, t_{cc} 37
3.5 Numerical Convergence 38

4 Conclusions & Outlook **43**

Bibliography **47**

List of Figures

1.1 A cartoon view of the general structure of a Spiral Galaxy. Taken from Anand et al 2021[8]. The labels were modified for demonstration purposes. This figure illustrates the key components of a galaxy's gaseous ecosystem, highlighting the dynamic interplay between the interstellar medium (ISM), the circumgalactic medium (CGM), and the intergalactic medium (IGM) through processes such as accretion, outflows, and recycling. 2

1.2 Sketch of the initial condition for the wind-cloud interaction problem, where the grey circle represents the cloud. The cloud is about to be impacted by a uniform supersonic wind, setting the stage for the complex dynamics explored in our simulations. Adapted from Sparre et al. 2018[9]. 3

2.1 Flowchart illustrating the modular workflow for post-processing simulation data, emphasizing shock identification, tracking, and visualization based on user-defined parameters. 9

2.2 Sketch of the left-to-right temporal evolution of the internal cloud shock to understand the function of the shock tracking module. The black shape represents the dense cloud that is deforming over time due to compression. The yellow curve is the internal shock, the red line is the last shock cell tracked and the blue line is the last dense cloud cell tracked. This figure demonstrates how the shock-tracking module adapts to the changing morphology of the internal shock and the dense cloud, accurately identifying the last shock cell even as the concavity reverses of the shock. 12

2.3 2D density slices on the XY plane at $z = 0$ pc and t = 0.00 Myr of the three wind-cloud models. Panel (a) shows a spherical sharp-edges model with a radius of 10 pc. Panel (b) the spherical sharp-edges model with a radius of 5 pc. Panel (c) illustrates the model with smoothed edges. This figure demonstrates the initial density distributions of the three cloud models, highlighting the differences in their size and edge definition. 14

3.1 2D slices at $z = 0$ pc, showing the evolution of the logarithm of the density in the (a) sharp-edges cloud $r_c = 10$ pc model. The evolution is shown in 5 different physical times: $t = 0.00, 0.36, 0.73, 1.10$ and 1.46 Myr. This figure demonstrates the progressive disruption and fragmentation of a sharp-edged cloud due to its interaction with a wind. 20

3.2 2D slices at z=0 pc, showing the evolution of the velocity in the in the (a) sharp-edges cloud $r_c = 10$pc model. The evolution is shown in 5 different physical times: $t = 0.00, 0.36, 0.73, 1.10$ and 1.46 Myr. This figure illustrates how the initially stationary cloud is accelerated and disrupted by the wind, leading to the formation of a turbulent wake and complex velocity structures. 21

3.3 2D slices at $z = 0$pc, showing the evolution of the logarithm of the density for cloud material in the three cloud models, (a), (b), (c). The evolution is shown in 5 different physical times: $t = 0.00, 0.36, 0.73, 1.10$ and 1.46 Myr. This figure highlights the distinct morphological evolution of clouds with different initial conditions as they interact with a wind. 23

3.4 Evolution of several cloud diagnostics for the three cloud models (smooth$_{10}$, sharp$_{10}$, sharp$_5$). Panels show: (a, b) effective cloud radii in X and Y directions, (c) center of mass displacement in Y, (d) mass-weighted velocity in Y, (e) mixing fraction, and (f) velocity dispersion in Y. This figure demonstrates the significant impact of initial cloud morphology on the dynamical and turbulent evolution of clouds in a wind-driven environment 26

3.5 2D slices at $z = 0$pc, showing the evolution of the velocity divergence in the the three cloud models, (a), (b), (c). The evolution is shown in 5 different physical times: $t = 0.00, 0.36, 0.73, 1.10$ and 1.46 Myr. Darker colors indicate convergent flow, while lighter colors represent divergent flow. Shock candidates are primarily associated with regions of strong convergence (darker colors). 28

3.6 2D slices at $z = 0$pc, showing the evolution of the pressure gradient in the the three cloud models, (a), (b), (c). The evolution is shown in 5 different physical times: $t = 0.00, 0.36, 0.73, 1.10$ and 1.46 Myr. 29

3.7 Mach number histograms for all computational domain of the three cloud models, (a), (b), (c). The evolution is shown in 4 different physical times: $t = 0.36, 0.73, 1.10$ and 1.46 Myr. This figure shows the temporal evolution of shock intensities in wind-cloud interactions, revealing a small number of subsonic cells, an initial plateau at $\mathcal{M} \approx 4$ and a progressive increase in shock intensity due to turbulence. 31

3.8 2D slices at $z = 0$pc, showing the evolution of the shock cells in the the three cloud models, (a), (b), (c). The evolution is shown in 5 different physical times: $t = 0.00, 0.36, 0.73, 1.10$ and 1.46 Myr. This figure visualizes the formation, propagation, and morphological changes of shocks within the clouds as they interact with the wind. 32

3.9 2D slices at $z = 0$pc, showing the evolution of the intern shock cells and the last shock cell detected in the the three cloud models, (a), (b), (c). The evolution is shown in 5 different times: $t = 0.00, 0.36, 0.73, 1.10$ and 1.46 Myr. The blue line indicates the position of the last internal shock cell detected by the shock tracking algorithm. 35

3.10 Temporal evolution of the last shock cell and last dense cloud of the three models: (a) sph-sharp$_{10}$, (b) sph-sharp$_5$, (c) sph-smooth$_{10}$. In each panel, there are three main elements: the blue line indicates the evolution of the last internal shock cell, becoming transparent after the shock reaches the cloud as it's no longer of interest; the red line shows the evolution of the last dense cloud cell; and the vertical dotted line represents the exact time when the shock reaches the back of the cloud, which is our numerical $t_{\rm cc}$. 36

3.11 Histogram of the distribution of $t_{\rm cc}$ values at t = 0.00 Myr of smooth$_{10}$ cloud. The graph shows a U-shaped distribution, where the right side corresponds to the denser center of the cloud, and the left side represents the edges of the cloud where the density is lower. 38

3.12 2D density slices on the XY plane at $z = 0$ pc and $t_{\rm cc} = 1$ Myr for the sharp$_{10}$ model at different resolutions. Panel (a) shows a model with a resolution of R$_{64}$. Panel (b) has R$_{32}$, panel (c) has R$_{16}$, and panel (d) has R$_8$. This figure illustrates the same model at the same time with different resolutions to show the qualitative differences between them. 39

3.13 Evolution of several cloud diagnostics for the sharp$_{10}$ model with different resolution. Panels show: a) cloud center of mass in Y, b) cloud velocity in Y, c) effective cloud radius in X, d) Velocity dispersion in Y. This figure demonstrates the significant impact of the resolution on the evolution of several cloud diagnostics. 41

List of Tables

2.1 Numerical solvers and methods used in PLUTO 8

2.2 Summary of initial conditions of the different cloud models. The table shows the model name (1), resolution (2), number of cells in each direction (3), domain size in parsecs (4), adiabatic index (5), density contrast (6), initial cloud radius (7), and wind Mach number (8). 15

3.1 Cloud crushing times ($t_{\rm cc}$) for the three cloud models, calculated using the analytical expressions by Klein et al. (1994) and Jones et al. (1996). 33

3.2 Cloud crushing times ($t_{\rm cc}$) for the three cloud models, calculated using the analytical expressions by Klein et al. (1994) and Jones et al. (1996), the numerical approximation and the relative errors $\epsilon_{\rm r}$ between each analytical expression and the numerical approximation. 37

3.3 Cloud-crushing time values, considering ten different ways of calculating it. 37

3.4 Relative errors of the cloud-crushing time values from numerical estimation, considering ten different ways of calculating it. 38

List of Papers

[1] Navarrete, S.; Pinargote, B. J.; Banda-Barragán, W. E. Shock waves in Interstellar Cloud-Cloud and Wind-Cloud Collisions. Journal of Physics: Conference Series 2024, 2796, 012005

Chapter 1

Introduction

1.1 Structure of spiral galaxies

Within the vast expanse of the Universe, a variety of galaxies exist, including elliptical, spiral, and those with irregular morphology. Each galaxy comprises vast conglomerates of stars, dust, gas and dark matter intricately bound together by the force of gravity. Located within one of these galaxies, our planet and Solar system are located in the Milky Way, a canonical spiral Galaxy with an approximate size of 31 kpc[10] and an estimated age of 13 Gyr[11]. The structural composition of the Milky Way, similar to that of its spiral counterparts, encompasses the Interstellar Medium (ISM), the Circumgalactic Medium (CGM), and the Intergalactic Medium (IGM) as shown in Figure 1.1.

In spiral galaxies, the medium between stars, along with everything it contains, constitutes what is known as the Interstellar Medium (ISM). The ISM constitutes one of the most crucial elements in galactic dynamics, as it plays a pivotal role in the formation of stars, which serve as the primary sources of energy and feedback processes[12]. The matter that makes up the ISM largely escapes direct visual detection, emitting predominantly in the radio and infrared wavelengths. Broadly speaking, the ISM comprises gas, dust, cosmic rays, electromagnetic radiation and magnetic fields[12]. Specifically, the gas and dust clouds within the ISM consist predominantly of hydrogen and helium, with traces of heavier atoms (knowns as metals) in various states, ionized, neutral, and molecular in gaseous or solid form.

Extending far beyond the visible galaxy disc, yet still gravitationally bound to the galaxy, there exists a diffuse medium enveloping the outskirts of the ISM, known as the Circumgalactic Medium (CGM) or galactic halo. CGM have a lower density than the ISM, but it still contains gas and stars. Thus, the CGM serves as a fuel reservoir for the star formation process occurring within a galaxy, playing an essential role in galactic feedback and in the recycling of gas and metals[13]. Additionally, it can be regarded as a crucial regulator in the supply of galactic gas, influencing the material cycles that sustain stellar activity and the evolutionary dynamics of the galaxy.

Although the edges of a galaxy cannot be fully defined, a commonly used boundary is the virial radius (the radius inside which the average density equals 200 times the critical density of the universe). The virial radius of the Milky Way Galaxy is approximately ~50 kpc[14]. Beyond this radius lies the Intergalactic Medium (IGM), filling in vast regions between galaxies. In this space, the influence of individual galaxies can be from negligible to extreme. For

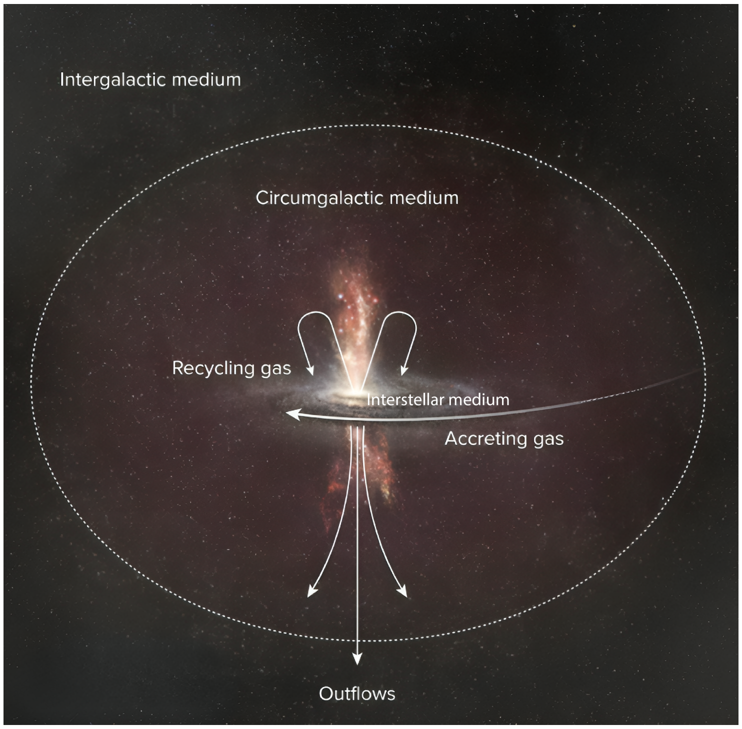

Figure 1.1: A cartoon view of the general structure of a Spiral Galaxy. Taken from Anand et al 2021[8]. The labels were modified for demonstration purposes. This figure illustrates the key components of a galaxy's gaseous ecosystem, highlighting the dynamic interplay between the interstellar medium (ISM), the circumgalactic medium (CGM), and the intergalactic medium (IGM) through processes such as accretion, outflows, and recycling.

large galaxies and those with strong outflows and active galactic nuclei, such influence has been recorded to extend deep into the IGM. Their impact on surroundings depends on factors such as mass, star formation rates, and outflows intensity. At larger scales, the IGM structure is determined primarily by gravitational fields of groups and clusters of galaxies and by the cosmic web filamentary and void structure[15].

The IGM contains mostly pristine hydrogen and helium from the early universe, with metal-enriched gas ejected from galaxies. The enriched component arises from a variety of sources, such as intense star formation, supermassive black hole activity (AGN), supernovae, and galaxy interactions. Such enrichment is non-linear, ranging from a higher concentration around galaxies and galaxy clusters to pristine regions in cosmic voids[15].

Despite the multifaceted nature of the constituents of galaxies, this thesis focuses on a specific scenario within the ISM: we study the collision between an interstellar gas cloud and a stellar-driven wind originating from e.g. isolated stars, star clusters, star-forming regions, and/or explosive events of dying stars (known as supernova explosions, SNe).

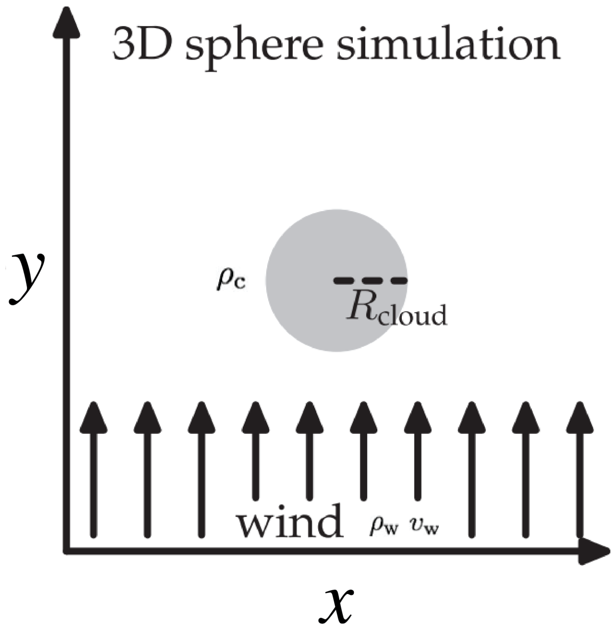

Figure 1.2: Sketch of the initial condition for the wind-cloud interaction problem, where the grey circle represents the cloud. The cloud is about to be impacted by a uniform supersonic wind, setting the stage for the complex dynamics explored in our simulations. Adapted from Sparre et al. 2018[9].

1.2 Wind-cloud systems in the ISM

It is essential to clearly define the model on which this work is based: the **wind-cloud model** (see Figure 1.2). This model represents an abstract scenario where a solitary and stationary interstellar cloud interacts with a wind moving at a specified velocity, all within a finite volume[16]. While this model may sound somewhat idealised, its simplicity makes it ideal for studying small-scale interactions, which are harder to isolate in more realistic scenarios. Indeed, wind-cloud models have been extensively studied to understand various interactions within the ISM[17 18 19 9].

One of the pioneering simulations in this field, was reported by Murray et al. (1993)[20]. Their study revealed the critical role of gravitational forces in stabilizing clouds against Kelvin-Helmholtz instabilities, highlighting the delicate balance between mass, self-gravity, and pressure in cloud stability. Building on this foundation, Klein et al. (1994)[2] and Xu & Stone (1995)[21] investigated cloud interactions with various symmetries and uniform density profiles with shock waves, demonstrating convergence in hydrodynamical simulations at resolutions of ~ 100 zones per cloud radius and observed the formation of highly complex filamentary structures.

As technology advanced, so did the sophistication of these simulations. Miniati et al. (1999)[22] use magnetic fields with different orientations, demonstrating how they can dramatically alter cloud dynamics, even converting magnetic energy into kinetic energy under certain conditions. Nakamura et al. (2006)[23] refined cloud models further, introducing smooth density distributions that more closely mirrored real interstellar clouds.

Later, Raga et al. (2007)[24] compared 2D and 3D models of radiative interstellar bullet flows, revealing crucial differences that underscored the necessity of 3D simulations for capturing the full complexity of these phenomena. This push towards realism continued with Vieser & Hensler (2007)[25], who incorporated heat conduction into their models, uncovering its protective effect against cloud destruction by Kelvin-Helmholtz instabilities.

The field expanded its scope with Cooper et al. (2009)[26], who simulated starburst-driven galactic winds interacting with nonspherical radiative clouds. Their work emphasized the critical role of radiative cooling and turbulent densities in cloud survival and filament formation, painting a more nuanced picture of galactic outflows. Scannapieco & Brüggen (2015)[27] further refined these models, revealing how supersonic flows create Mach cones around clouds and establishing key scaling relationships for cloud evolution.

Later, Pittard & Parkin (2016)[28] conducted HD simulations of adiabatic shock-cloud interactions, varying shock Mach numbers and cloud density contrasts. They compared 2D and 3D results, performed resolution tests, and examined the effects of a subgrid turbulence model. Their work revealed that 32-64 cells per cloud radius are necessary for capturing key dynamics in 3D interactions and found little difference between 2D and 3D simulations in terms of cloud lifetime and acceleration. Banda-Barragán et al. (2019)[29] pushed the boundaries of cloud modeling by incorporating turbulent density distributions with different log-normal density distributions. Their work revealed that the internal structure of clouds significantly influences the evolution and survival of clouds immersed in galactic winds, adding another layer of complexity to our understanding of the ISM and CGM.

The ongoing research in wind-cloud models continues to unveil new insights and raise intriguing questions within the field. Our work contributes an additional piece to the complex puzzle that scientists around the world have been assembling over the last few decades. The collective effort is pointed toward deepening our understanding of the physical processes that occur within ISM. With every new exploration, we are thus further going into understanding the mystery of wind-cloud interaction in the ISM, thereby reaching a step closer to a complete picture of these complex astrophysical systems.

1.3 Problem Statement

The accurate modeling of baryonic matter remains a significant challenge in astrophysical simulations, affecting our understanding of various cosmic phenomena, from galactic evolution to star formation. A crucial aspect of this challenge lies in correctly simulating the interactions between different phases of the interstellar and circumgalactic media, particularly in wind-cloud scenarios. These interactions play a vital role in processes such as galactic outflows, cloud disruption in the ISM, and the mixing of multi-phase gas in different temperature regimes. Within this context, a key parameter in wind-cloud simulations is the cloud-crushing time (t_{cc}).

The t_{cc}, is the characteristic time for an internal shock to traverse a cloud, and it represents the timescale of cloud disruption. The widely used formula for t_{cc} was proposed by Klein et al. (1994)[2]:

$$t_{\mathrm{cc}} \equiv \frac{\chi^{1/2} r_c}{v_w}, \tag{1.1}$$

where r_c is the cloud radious, v_w is the typical internal post-shock velocity and χ is the density contrast between the cloud and the inter-cloud background medium:

$$\chi \equiv \frac{\rho_{c0}}{\rho_{i0}}. \tag{1.2}$$

Similarly, Jones et al. (1994[1], 1996[30]) defined the $t_{\rm cc}$ by taking into account the cloud diameter instead of the radius:

$$t_{\rm cc} = \frac{2r_{\rm c}}{v_{\rm s}} = \left(\frac{\rho_{\rm c}}{\rho_{\rm w}}\right)^{1/2} \frac{2r_{\rm c}}{\mathcal{M}_{\rm w}c_{\rm w}} = \chi^{1/2}\frac{2r_{\rm c}}{\mathcal{M}_{\rm w}c_{\rm w}}, \tag{1.3}$$

where $v_s = \mathcal{M}_{\rm w}c_{\rm w}\chi^{-\frac{1}{2}}$ is the approximate speed of the internal shock travelling through the cloud after the initial collision with the wind. Here, $\mathcal{M}_{\rm w} = \frac{|v_{\rm w}|}{c_{\rm w}}$ is the Mach number of the wind, and $c_{\rm w} = \sqrt{\gamma\frac{P_{\rm th}}{\rho_{\rm w}}}$ is the sound speed in the wind medium.

It is significant to remember that the original equation was derived on 2D and 2.5D simulations, even if it has been demonstrated that this timescale offers an acceptable approximation for a variety of simulation types. Moreover, it was designed especially for steady, planar shocks interacting with spherical clouds, ignoring source terms (such as self-gravity, magnetic fields, and electron thermal condution) and their internal structure. These drawbacks in the original derivation cast doubt on its generalizability, especially in increasingly intricate 3D scenarios involving more physical processes. Because of the variations amongst simulations, the authors actually mention several approaches to this time-scale in a number of papers. Some authors[19] [31] opt for eq. 1.1, while others[32] [33] opt for eq. 1.3.

The validity of this formula in more complex 3D environments has not been thoroughly examined. This thesis aims to critically assess the universality and potentially reformulate the $t_{\rm cc}$ equation through 3D simulations. By revisiting this standard metric, we seek to contribute to the study of wind-cloud interaction models in the ISM (and CGM), which is essential for a more precise understanding of astrophysical processes ranging from small-scale cloud dynamics to large-scale galactic evolution.

1.4 General and Specific Objectives

The aim of this thesis is to understand the mechanisms influencing the formation of shock waves and associated time scales in galactic wind-cloud interactions. Through numerical simulations, the study aims to track and characterize internal shocks within these systems, with a specific focus on quantitatively measuring the the cloud-crushing time. Furthermore, our research seeks to compare the numerical results with existing analytical predictions, and adjust the $t_{\rm cc}$ equations (1.1, 1.3) in the event of observed discrepancies. To achieve this objective, the following specific goals need to be achieved:

- Perform hydrodynamic (HD) simulations of wind clouds with different initial conditions.
- Design and implement a robust algorithm that can track the identification of any internal or external shocks in simulations of winds and clouds.
- Characterize identified shocks by looking at their properties and interactions, such as Mach number, density, and pressure jumps, and follow their evolution over time in a simulated environment.

- Quantitatively measure the cloud-crushing time associated with internal shocks.
- Conduct a comprehensive comparative analysis between the numerically calculated $t_{\rm cc}$ values and those derived from existing analytical prescriptions.
- Refine and correct the mathematical equation governing the calculation of $t_{\rm cc}$ based on the observed disparities between numerical simulations and analytical predictions.
- Assess the implications of the refined $t_{\rm cc}$ equation for our understanding of cloud survival and evolution in galactic winds and other astrophysical contexts.

Chapter 2

Methodology

This chapter outlines the methodologies employed in this study to simulate, analyze, and visualize the interactions between stellar-driven winds and interstellar clouds, particularly focusing on the cloud-crushing time ($t_{\rm cc}$). To achieve this, we used numerical simulations in which a supersonic wind interacts with an isolated cloud under certain initial conditions. The methodology encompasses the simulation setup using the PLUTO code, our post-processing tools developed for data analysis and visualization, and the hardware resources utilized for running the simulations. All elements used in this work are described below.

2.1 Numerical setup of the PLUTO code:

We have utilized PLUTO, a numerical simulation code widely used in the astrophysical community. Developed by Mignone et al. (2007)[3], PLUTO is an open-source package designed to solve systems of hyperbolic and parabolic equations describing astrophysical gas dynamics. PLUTO offers modules for hydrodynamics (HD), magnetohydrodynamics (MHD), relativistic hydrodynamics (RHD), and relativistic magnetohydrodynamics (RMHD), allowing its application in a wide range of astrophysical scenarios, from star formation to galactic winds and shock waves. Its versatility extends to its execution capability, able to run on both individual workstations and supercomputing facilities with thousands of processors, thanks to its parallelization using the Message Passing Interface (MPI). This flexibility, combined with its numerical stability and robustness, makes PLUTO an ideal tool for our study of wind-cloud interactions in galactic environments.

PLUTO is primarily written in C for performance, with a user-friendly Python interface for problem setup. It implements Godunov-type shock-capturing schemes using finite-volume/finite-difference techniques. This structure combines computational efficiency with ease of use, allowing flexible customization of simulations without extensively modifying the core codebase.

PLUTO operates with both conservative and primitive variables, employing a dual approach to simulate fluid dynamics. The code evolves the system over time by solving a set of conservation laws, defined by the conservative variables $U = (\rho, m, E)^T$, where ρ is density, m is momentum and E is total energy. These conservation laws are explicitly formulated in equations 2.1, 2.2, 2.3, and 2.4. Complementary, PLUTO uses primitive variables $V = (\rho, v, p)^T$, where v is velocity and p is pressure, to specify initial and boundary conditions. These conditions, crucial for defining the properties of the cloud and the surrounding medium, are established in the *init.c* file.

We solved with PLUTO v4.4 pure HD equation on uniform static grids in a 3D Cartesian coordinate system (X, Y, Z). In this HD model, the conservation laws for mass, momentum, and energy are solved using finite-volume methods:

$$\frac{\partial \rho}{\partial t} + \boldsymbol{\nabla} \cdot [\rho \boldsymbol{v}] = 0, \tag{2.1}$$

$$\frac{\partial [\rho \boldsymbol{v}]}{\partial t} + \boldsymbol{\nabla} \cdot [\rho \boldsymbol{v}\boldsymbol{v} + \boldsymbol{I}P] = 0, \tag{2.2}$$

$$\frac{\partial E}{\partial t} + \boldsymbol{\nabla} \cdot [(E + P)\, \boldsymbol{v}] = 0, \tag{2.3}$$

$$\frac{\partial [\rho C]}{\partial t} + \boldsymbol{\nabla} \cdot [\rho C \boldsymbol{v}] = 0, \tag{2.4}$$

where ρ is the mass density, $\boldsymbol{v}$ is the velocity, $P = (\gamma - 1)\,\rho\epsilon$ is the gas thermal pressure (ideal equation of state with $\gamma = 5/3$ for adiabatic simulations), $E = \rho\epsilon + \frac{1}{2}\rho \boldsymbol{v}^{\mathbf{2}}$ is the total energy density, ϵ is the specific internal energy, and C is a Lagrangian scalar that allows us to track gas material (at time $t = 0$, $C = 1$ inside the multicloud layer, and $C = 0$ everywhere else), it is named as the cloud tracer (tr1).

Additionally, to solve the hyperbolic differential equations, we utilized the TDVLF approximate Riemann solver, which uses a Lax-Friedrichs scheme[34]. It prevents the occurrence of negative pressures and densities that can create numerical instabilities. For time discretization, we employed a third-order Runge-Kutta (RK3) method for better stability properties. Furthermore, we implemented a parabolic reconstruction method for spatial discretization. Specifically, we used a piece-wise Total Variation Diminishing (TVD) parabolic reconstruction applied to the primitive variables. This method is second-order accurate in space and utilizes a three-point wide stencil to ensure stable and accurate results. To ensure the stability of the numerical scheme, we adhered to the Courant-Friedrichs-Lewy (CFL) condition with a value of 0.33. The CFL condition dictates the maximum allowable time step for the simulation based on the grid size and the wave speeds, preventing numerical instabilities and ensuring the accuracy and convergence of the simulation results. In summary, we have:

Component	**Method/Parameter**
Riemann Solver	TVDLF
Time Discretization	RK3
Spatial Reconstruction	Parabolic
CFL Number	0.33

Table 2.1: Numerical solvers and methods used in PLUTO

2.2 Post-processing (data analysis and visualization) tools:

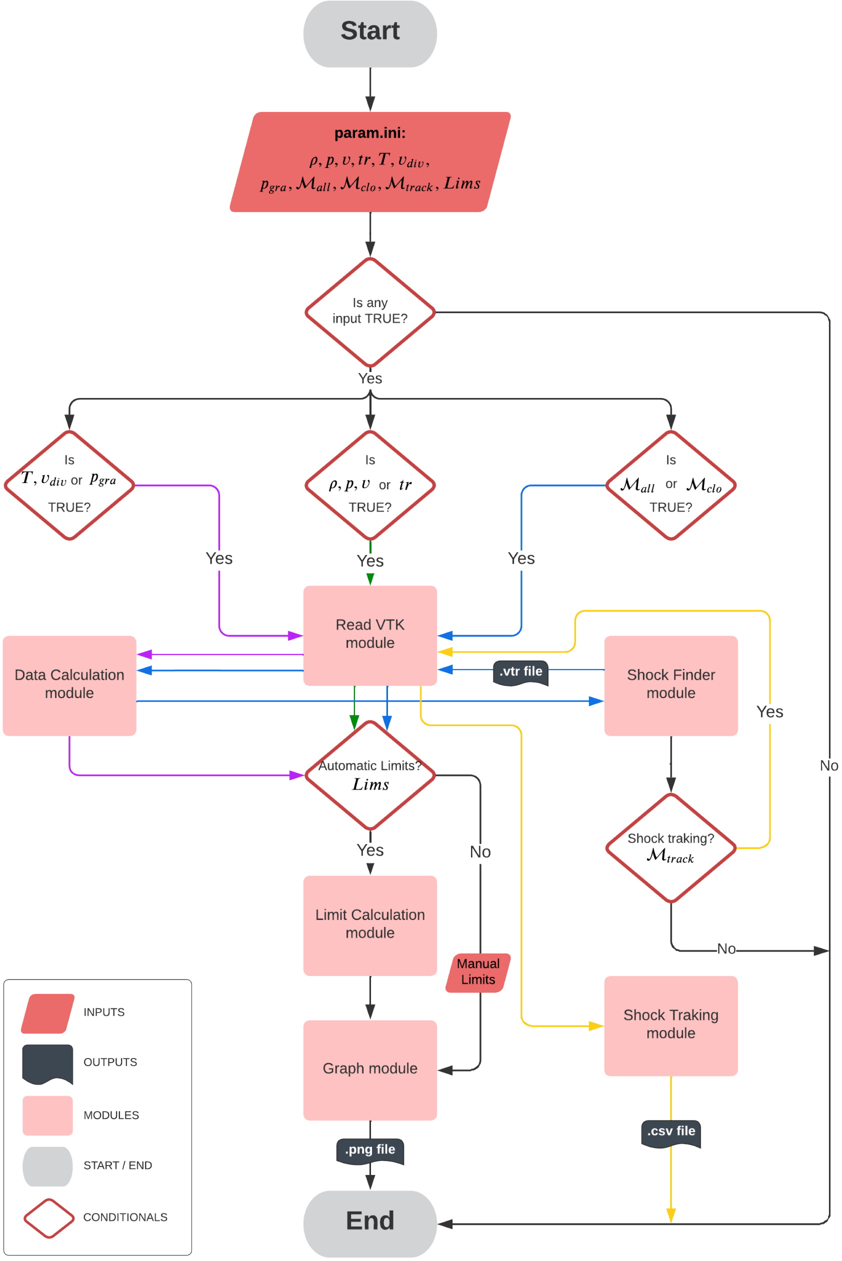
Start
param.ini:
$\rho, p, v, tr, T, v_{div},$
$p_{gra}, \mathcal{M}_{all}, \mathcal{M}_{clo}, \mathcal{M}_{track}, Lims$
Is any input TRUE?
Yes
No
Is T, v_{div} or p_{gra} TRUE?
Is ρ, p, v or tr TRUE?
Is $\mathcal{M}_{all}$ or $\mathcal{M}_{clo}$ TRUE?
Yes
Yes
Yes
Read VTK module
Data Calculation module
.vtr file
Shock Finder module
Yes
Automatic Limits? $Lims$
Yes
No
Shock traking? $\mathcal{M}_{track}$
No
Limit Calculation module
Manual Limits
Shock Traking module
Graph module
.png file
.csv file
End
INPUTS
OUTPUTS
MODULES
START / END
CONDITIONALS

Figure 2.1: Flowchart illustrating the modular workflow for post-processing simulation data, emphasizing shock identification, tracking, and visualization based on user-defined parameters.

This section details the primary modules employed in the detection and tracking of shock cells. These modules were programmed entirely in Python 3.13. Figure 2.1 illustrates the utilized workspace, where the various developed modules are highlighted in pink. The "Read VTK" module is responsible for reading and extracting data from any .vtk and/or .vtr file. The .vtk files, which are structured grid data files, are generated at each time step of the simulations. They contain information about density, velocity, pressure, and the cloud tracer.

The "Data Calculation" module calculates temperature, velocity divergence, and pressure gradient based on the data extracted from the .vtk files of the simulation and the requirements of the user. Furthermore, we have the "Shock Finder" module, which identifies shock cells within the simulation using data from both the "Data Calculation" and "Read VTK" modules. It generates .vtk files for each simulation time step, containing information about internal and external shocks within the cloud. Another crucial module is the "Shock Tracking" module, which tracks both the internal shock and the dense cloud, producing a .csv file with these values. Lastly, we have two additional modules: "Limit Calculation" and "Graph." These are closely linked, as the former, if required by the user, automatically calculates appropriate limits for plotting the simulation. The "Graph" module then formats and generates the requested images.

2.2.1 I/O python functions:

The created module is designed to read .vtk files from PLUTO simulations, extracting values for density (ρ), thermal pressure (p), velocity in each direction (v_{x1}, v_{x2}, v_{x3}), and the cloud tracer (tr1). Additionally, normalization units are read from the pluto.log.0 file, and the time for each .vtk file is retrieved from vtk.out.

Based on the requirements of the user, the module can output three types of files: The first one (1) .png images at each timestep, visualizing the parameter specified by the user. The second option (2), if the user opts to graph the shock cells, the module also outputs .vtr files containing information about the shock cells within the cloud and throughout the computational domain. As a third (3) option the module can produce a .csv file with data on the final position of the shock and the cloud, which is essential for calculating the t_{cc}. In summary, the functionality of the module can be characterized by its inputs and outputs:

Inputs:

- .vtk files: Containing simulation data for each timestep
- pluto.log.0: Provides normalization units
- vtk.out: Contains time information for each .vtk file

Outputs:

- .png images: Visualizations of user-specified parameters at each timestep
- .vtr files: Data on shock cells within the cloud and computational domain
- last_position.csv: Contains data on the final positions of the shock and cloud, crucial for t_{cc} calculations

2.2.2 Our Shock Finder Python module:

The Mach number, a dimensionless quantity, represents the local flow speed of gas in units of the sound speed. Shock waves are characterized by Mach numbers greater than one. A crucial step to achieve our goals is to identify the shocked cells and determine their Mach numbers. Our Shock Finder module relies on the Rankine-Hugoniot (RH) jump conditions[35], which describe the behavior of a gas across shock discontinuities based on the specific heat capacity ratio γ and the shock Mach number. From these conditions, we utilise the following equation:

$$M_{x,y,z} = \frac{-\nabla v_{x,y,z}(1+\gamma) + \sqrt{16c_s^2 + \nabla v_{x,y,z}^2(1+\gamma)^2}}{4c_s}, \tag{2.5}$$

where $\nabla v_{x,y,z}$ represents the directional velocity gradient, and $c_s = \sqrt{\gamma \frac{P}{\rho}}$ is the sound speed. A more detailed derivation of this equation can be found in Navarrete (2023)[36] and Teutloff (2021)[37]. Following the algorithm by Vazza et al. (2011), we search for abrupt changes in flow variables, such as density or pressure. In summary, our Shock Finder module operates according to the following routine[38]:

- Read the VTK files.
- Calculate the velocity divergence $\vec{\nabla} \cdot \vec{v} < 0$
- Calculate the pressure gradient $|\vec{\nabla} p| > \Pi$.
- Tag shock wave candidate cells that satisfy both conditions using cloud trackers.
- Calculate the sound speed in each cell $c_s = \sqrt{\gamma \frac{P}{\rho}}$
- Find the minimum c_s in nearby cells.
- Calculate the Mach number in each cell.
- Combine Mach numbers and tagged cells.

In our shock detection approach, we employ a criterion that focuses on normalized pressure gradients exceeding $\Pi = 0.1$. This threshold serves to eliminate discontinuities with minimal pressure changes, which are more characteristic of subsonic waves rather than true shocks.

It must also be mentioned that this module has been enhanced from the past versions to generate Mach number files both inside and outside the cloud together in .vtr files. The file formats .vtr/.vtk are very popular within the realms of astrophysics and fluid dynamics, being able to represent very complex volumetric and geometric data, easily visualized from a scientific point of view, compatible with corresponding analyzing tools, as ViSIt. Finally, this module has been parallelized using *multiprocessing* library provided by Python, thus further improving the load times and processing times for the application. This increases efficiency as it cuts down the time it takes to read and process the information.

2.2.3 Shock tracking routine for the internal cloud shock:

The shock tracking module processes volumetric data stored in .vtk/.vtr formats, extracting scalar fields including density, tracer concentrations, and internal shocked cells. This module employs a density threshold of $\rho \geq \rho_{max,0}/2$ to identify and follow the densest parts of the cloud, where $\rho_{max,0}$ represents the initial maximum density of the cloud. For shock detection, the module identifies internal shocks by considering cells with Mach numbers $\mathcal{M} \geq 3$, ensuring the capture of genuine internal shocks while excluding those formed by instabilities or secondary interactions.

For each simulation time step, the module performs a planar cut through the mid-plane. It then systematically analyzes this 2D slice, traversing column by column to locate the last cell of the dense cloud and the furthest extent of internal shocks. This process involves storing the highest value data points for both the cloud density and shock Mach number criteria. The maximum values across all columns represent the farthest extent of the dense cloud and internal shock for that simulation time. By repeating this analysis for each time step, the module constructs a comprehensive temporal evolution of both the trailing edge of the dense cloud and the internal shocks over time.

When the furthest shocked cell reaches the trailing edge of the dense cloud we consider this time as our numerical estimate of the t_{cc}. Figure 2.2 shows a cartoon schematic of how the internal shock is tracked. In the image, the dense cloud is in black and the internal shock in white. The red line indicates the furthest extent of the shock according to our tracking routine.

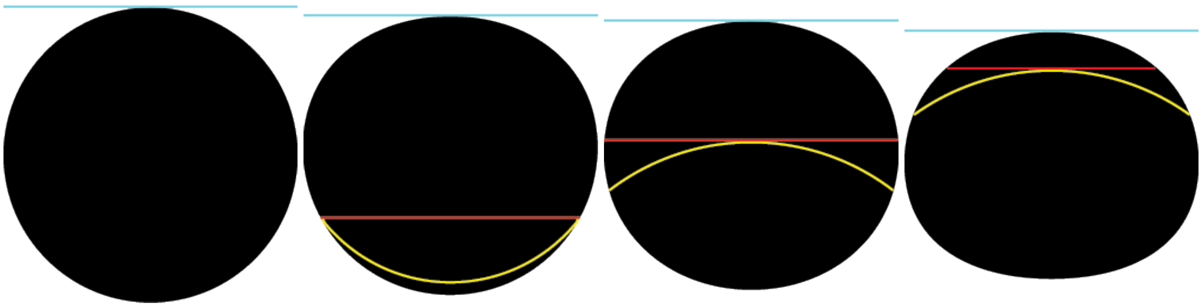

(a) Initial cloud. (b) Internal convex shock. (c) Internal concave shock. (d) Far internal concave shock.

Figure 2.2: Sketch of the left-to-right temporal evolution of the internal cloud shock to understand the function of the shock tracking module. The black shape represents the dense cloud that is deforming over time due to compression. The yellow curve is the internal shock, the red line is the last shock cell tracked and the blue line is the last dense cloud cell tracked. This figure demonstrates how the shock-tracking module adapts to the changing morphology of the internal shock and the dense cloud, accurately identifying the last shock cell even as the concavity reverses of the shock.

2.3 Computational Requirements

The initial code development and preliminary testing were conducted on a personal workstation with a 10-core, 16-thread processor and 16 GB of RAM. This setup was crucial for script development, debugging, and small-scale concept testing before scaling up to more powerful systems.

For large-scale simulations, we primarily utilized the SuperMUC-NG at the Leibniz Supercomputing Centre (LRZ) in Germany. We configured jobs on the ’micro’ and ’general’ partitions, using 16-20 nodes with 48 tasks per node, totaling 768-960 cores for parallel processing. This setup was critical for our high-resolution 3D HD simulations. Each simulation typically ran for approximately 6 hours, highlighting the computational intensity of our work. A key aspect of our strategy was the implementation of domain decomposition, specified in the SBATCH script. This technique divides the computational domain into subdomains, optimizing workload distribution across processors, and improving overall simulation efficiency.

We also leveraged the CEDIA HPC cluster in Ecuador, specifically utilizing the ’cpu-max’ partition. This configuration provided us with up to 128 CPU cores and 256 GB of RAM, which we employed for medium-resolution (R_{16}) and 2D simulations for preliminary analyses. The CEDIA resources were particularly valuable for conducting initial tests and analyses before moving to full-scale simulations on SuperMUC-NG.

Our computational workflow was managed through the SLURM workload manager, ensuring efficient use of HPC resources. The total storage required for the final simulations was approximately ≈ 2.0 TB. This multi-faceted approach to high-performance computing, utilizing international, national, and personal resources, was instrumental in achieving our research goals.

2.4 Simulation setup and models

2.4.1 Initial conditions

We simulate three main wind-cloud models where clouds are initially centered in the position (0, 0, 0) of the simulation domain, a position that serves multiple critical purposes. Additionally, three low resolution simulations were carried out to perform a numerical convergence analysis. The cloud is situated sufficiently low to ensures the complete capture and evolution of the bow shock formed by the wind-cloud interaction, while its central positioning provides symmetry advantages that facilitate easier analysis and interpretation of cloud deformation and surrounding flow patterns. Crucially, the cloud is maintained at an adequate distance from the lower boundary, a spacing that prevents the development and interference of reverse flows that could potentially contaminate the simulation results. This carefully considered positioning not only allows for extended tracking of the evolution of the cloud, but also ensures that all relevant physical processes are captured while computational artifacts are minimized.

The wind that interacts with the cloud is on the Y-axis with a uniform velocity field with a speed given by the Mach number and the wind sound speed: $v_{\rm w} = \mathcal{M}_{\rm w} c_{\rm w} = 4.0$. All three cloud models are spherical. However, two are completely symmetrical spheres with sharp edges (i.e. with a uniform density distribution) $\rho(r) = \rho_c$ for $r <= r_c$. The third model includes a sphere but with a smoothed density distribution (i.e. dense in the core and gradually dispersed towards the edges), modeled by:

$$\rho(r) = \rho_{\rm w} + \frac{(\rho_c - \rho_{\rm w})}{1 + \left(\frac{r}{r_{\rm core}}\right)^N}, \tag{2.6}$$

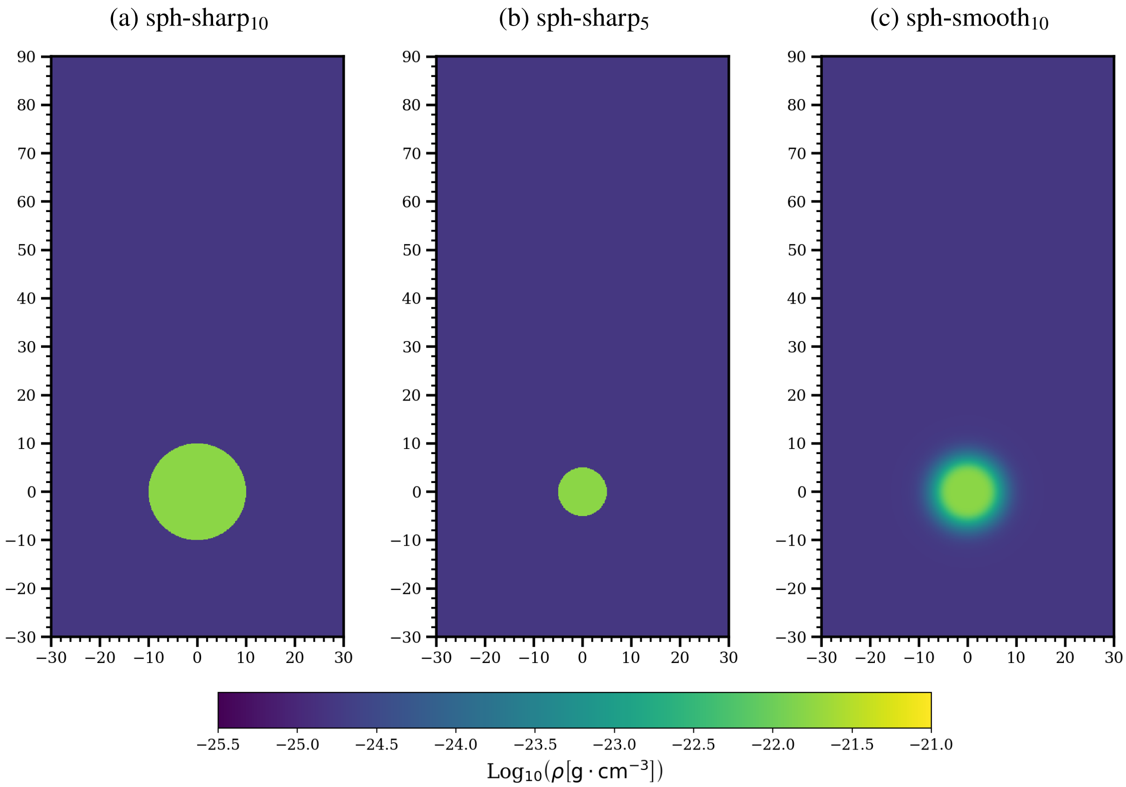

Figure 2.3: 2D density slices on the XY plane at z = 0 pc and t = 0.00 Myr of the three wind-cloud models. Panel (a) shows a spherical sharp-edges model with a radius of 10 pc. Panel (b) the spherical sharp-edges model with a radius of 5 pc. Panel (c) illustrates the model with smoothed edges. This figure demonstrates the initial density distributions of the three cloud models, highlighting the differences in their size and edge definition.

where $\rho_c = 100$ is the density at the center of the cloud, $\rho_w = 0.1$ is the density of the wind, $r_{\mathrm{core}} = 0.5$ is the radius of the cloud core, and N = 10 is an integer that determines the steepness of the curve describing the density gradient[23]. However, the density profile modeled by the Equation 2.6 extends to infinity, so an arbitrary boundary for the cloud is necessary: $r_{\mathrm{cut}} = 1.58$, at which $\rho\,(r_{\mathrm{cut}}) = 1.01\rho_{\mathrm{w}}$, and a boundary of the cloud at radius $r_{\mathrm{c}} = 1$ where $\rho\,(r_{\mathrm{c}}) = 2.0\rho_{\mathrm{w}}$

Additionally, all simulations utilize Cartesian coordinates with physical dimensions of $\mathrm{X}_1 = (-30, 30)$ pc, $\mathrm{X}_2 = (-30, 90)$ pc, and $\mathrm{X}_3 = (-30, 30)$ pc. The resolution of each simulation is determined by the number of cells that span the radius of the cloud, as exemplified in the first model sph-sharp$_{10}$ with R_{64}, indicating 64 cells across the cloud radius.

The initial conditions are summarized in Table 2.2 and graphically in Figure 2.3.

(1) Model	(2) Resolution	(3) Number of cells	(4) Domain (pc)	(5) γ	(6) χ	(7) r_c (pc)	(8) $\mathcal{M}_\mathrm{w}$
sph-sharp$_{10}$	R_{64}	$384 \times 768 \times 384$	$60 \times 120 \times 60$	$5/3$	10^3	10.0	4.0
sph-sharp$_{10}$-lr	R_{32}	$192 \times 384 \times 192$	$60 \times 120 \times 60$	$5/3$	10^3	10.0	4.0
sph-sharp$_{10}$-vlr	R_{16}	$96 \times 192 \times 96$	$60 \times 120 \times 60$	$5/3$	10^3	10.0	4.0
sph-sharp$_{10}$-vvlr	R_{8}	$48 \times 96 \times 48$	$60 \times 120 \times 60$	$5/3$	10^3	10.0	4.0
sph-sharp$_{5}$	R_{32}	$384 \times 768 \times 384$	$60 \times 120 \times 60$	$5/3$	10^3	5.0	4.0
sph-smooth$_{10}$	R_{64}	$384 \times 768 \times 384$	$60 \times 120 \times 60$	$5/3$	10^3	10.0	4.0

Table 2.2: Summary of initial conditions of the different cloud models. The table shows the model name (1), resolution (2), number of cells in each direction (3), domain size in parsecs (4), adiabatic index (5), density contrast (6), initial cloud radius (7), and wind Mach number (8).

2.4.2 Boundary conditions

The simulations are conducted within a 3D computational domain, augmented by four ghost zones along each axis. This configuration is specifically tailored to meet the requirements of the parabolic reconstruction algorithm employed in our numerical scheme. Five of the six domain boundaries implement outflow conditions, enforcing zero-gradient constraints at the computational box edges by replicating the values from the last active cell into the adjacent ghost cells. This approach effectively allows material to exit the computational domain without introducing spurious reflections. The bottom boundary is uniquely designated as an inflow condition (injection zone), ensuring that the vector fields in the first cell layer consistently point upward. This prevents the development of reverse flows that could contaminate the simulation with computational artifacts.

2.5 Diagnostics

To study the evolution of cloud models and their shock cells, various diagnostics can be calculated from the simulated data, including geometric, kinetic, and turbulence parameters. These parameters are calculated using discrete integrals of global quantities over the computational domain. The mass-weighted volume average, denoted by angle brackets $\langle\,\rangle$, is defined as:

$$\langle \mathcal{G} \rangle = \frac{\int \mathcal{G} \rho \, C \, \mathrm{d}V}{\int \rho \, C \, \mathrm{d}V}, \tag{2.7}$$

where $\mathcal{G}$ is any scalar variable from the simulation, and V is the volume. The denominator in this expression represents the time-dependent cloud mass. Similarly, the volume-average, denoted by square brackets [ ], is defined as:

$$[\mathcal{F}] = \frac{\int \mathcal{F}\, C\, \mathrm{d}V}{\int C\, \mathrm{d}V}, \tag{2.8}$$

where $\mathcal{F}$ is the value of the quantity being averaged. Here, the denominator represents the cloud volume. In the discrete form used in the simulations, these integrals become sums over the computational cells.

2.5.1 Cloud geometry

To quantify changes in the shape of the cloud during its collapse, we calculate the effective radius along each of its axes (X, Y, and Z). This allows us to track how the cloud elongates or flattens over time. Using Equation 2.7, we define $\langle \mathrm{X}_j \rangle$ as the averaged cloud extension along the j-th axis (the subscript j, where j can be 1, 2, or 3, denotes the direction along the X, Y, or X axis, respectively), and $\langle \mathrm{X}_j^2 \rangle$ as the root mean square of the extension of the cloud along the same axis. Then, the effective cloud radius is defined as follows[2]:

$$\iota_j = \left[5\left(\langle X_j^2\rangle - \langle X_j\rangle^2\right)\right]^{1/2}. \tag{2.9}$$

2.5.2 Cloud dynamics

It is also important to analyze the dynamics of the cloud to differentiate the impact of the wind on the cloud. To achieve this, we calculate the displacement of the center of mass of the cloud along the streaming axis, Y, with the Equation 2.7:

$$\langle d_y \rangle = \frac{\int Y \rho\, C\, \mathrm{d}V}{\int \rho\, C\, \mathrm{d}V}. \tag{2.10}$$

Similarly, we define $\langle v_y \rangle$ as the average mass-weighted velocity of the cloud along the streaming axis, Y:

$$\langle v_y \rangle = \frac{\int v_y \rho\, C\, \mathrm{d}V}{\int \rho\, C\, \mathrm{d}V}, \tag{2.11}$$

where v_y is the velocity component along the Y-axis.

2.5.3 Turbulence parameters

To understand the turbulent properties of the cloud material, we use the mixing fraction, which measures the degree of mixing between cloud and wind gas, expressed as a percentage (Xu & Stone, 1995[21]):

$$f_{\mathrm{mix,cloud}} = \frac{\int \rho\, C^*\, \mathrm{d}V}{M_{\mathrm{cloud,0}}}, \text{ with } C^*_{\mathrm{cloud}} := \{0.1 \le C_{\mathrm{cloud}} \le 0.9\}, \tag{2.12}$$

where C^* is a modified tracer that selects cells with a mixing fraction between 0.1 and 0.9, indicating partial mixing. $M_{\mathrm{cloud,0}}$ is the initial cloud mass.

In a similar way to the effective cloud radius (Equation 2.9), we use the velocity dispersion to characterize the turbulent velocities within the cloud (Mac Low et al. 1994[39]):

$$\delta_{v_j} = \sqrt{\langle v_j^2 \rangle - \left\langle v_j \right\rangle^2}, \tag{2.13}$$

$\langle v_j^2 \rangle$ and $\langle v_j \rangle$ are the mean square and average velocities along the jth axis, respectively.

Chapter 3

Results & Discussion

In this chapter we describe the analysis of the numerical simulation results for complex wind-cloud interactions. We start with a general description of the evolution of the wind–cloud systems by morphological transformation and kinematic behavior, which includes the development of turbulence inside the clouds. Below, we detail how the initial cloud morphology greatly influences these evolutionary process, compare and contrast the behaviors of clouds with different sizes and edge profiles. Further sections present a close look at the emerging shock structures, identify/characterize these shocks through the use of both divergence and pressure gradient information. We finally turn to the shock-tracking method for numerical estimates of cloud-crushing time, and to consider the range of applicability for the important timescale predicted by the analytical approximation.

3.1 Evolution of wind-cloud systems

The interaction between the wind and the cloud, as illustrated in Figure 3.1, leads to gradual disruption and elongation of the cloud over time, primarily along the direction of the wind flow. This process is driven by Kelvin-Helmholtz[40 41] (KH) and Rayleigh-Taylor[42 43] (RT) instabilities. The evolution of cloud density, shown in Figure 3.1, reveals the formation of intricate structures due to these instabilities, including prominent, high-density filaments that extend into the lower-density surrounding medium. Notably, the compression caused by the wind of material at the leading edge of the cloud results in a localized increase in density, while a distinct low-density wake forms behind the cloud as its envelope is stripped of its material. The cloud, initially spherical, progressively exhibits a deformation due to the compressive force of the wind.

The wind-cloud interaction also induces significant changes in the velocity field, as depicted in Figure 3.2. Initially, the velocity field is relatively uniform, except for the stationary cloud, which creates a distinct region of zero velocity. As the wind impacts the cloud, high-velocity regions emerge at the leading edge of the cloud, signifying the formation of a bow shock. The bow shock not only intensifies over time but it also expands laterally, enveloping a larger portion of the cloud. Behind the cloud, a turbulent wake develops, characterized by a complex interplay of high- and low-velocity regions. Velocity gradients become more emphasized with time, and the velocity field

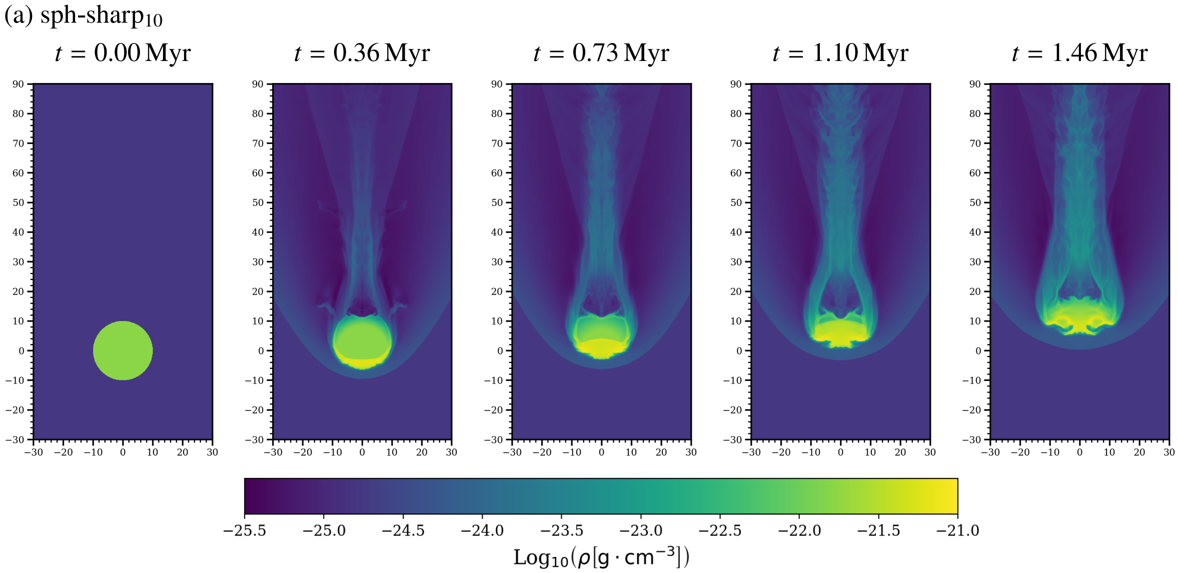

Figure 3.1: 2D slices at $z = 0$ pc, showing the evolution of the logarithm of the density in the (a) sharp-edges cloud $r_c = 10$ pc model. The evolution is shown in 5 different physical times: $t = 0.00, 0.36, 0.73, 1.10$ and 1.46 Myr. This figure demonstrates the progressive disruption and fragmentation of a sharp-edged cloud due to its interaction with a wind.

in its complexity increases with time as the simulation unfolds, relating to the evolution of turbulent structures and vortices. Our simulations align with previous numerical investigations that characterize the disruption of a cloud by a shock or wind as a four-stage process (Nittmann et al. 1982[44]; Klein et al. 1994[2]; Banda-Barragán et al. 2016[16]). These stages are as follows:

- **Compression:** The impact of the wind on the cloud generates a bow shock in the wind and transmits a shock into the cloud. This stage is crucial for characterizing the $t_{\rm cc}$. This compression, evident in the early stages of Figure 3.1, increases the density of the cloud and sets the stage for the subsequent interactions that ultimately lead to the disruption of the cloud.

- **Stripping:** KH instabilities form at the wind-cloud interface, stripping away the outer layers of the cloud. This is visible in the progressive loss of material from the edges of the cloud in the second and third panels of the top row of Figure 3.2 the stripped material is then carried downstream, contributing to the formation of the filamentary tail.

- **Expansion:** The transmitted shock propagates through the cloud, depositing energy and causing the cloud to expand. This is observable in the increased cloud size and the more diffuse appearance of the cloud material in the later snapshots of Figure 3.1.

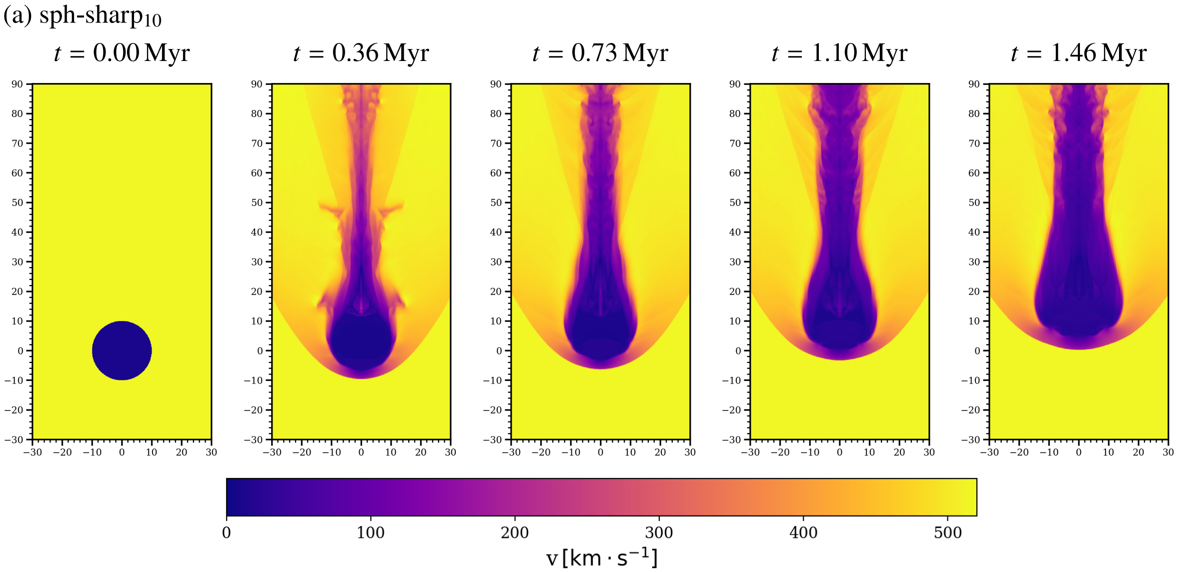

Figure 3.2: 2D slices at z=0 pc, showing the evolution of the velocity in the in the (a) sharp-edges cloud r_c = 10pc model. The evolution is shown in 5 different physical times: t = 0.00, 0.36, 0.73, 1.10 and 1.46 Myr. This figure illustrates how the initially stationary cloud is accelerated and disrupted by the wind, leading to the formation of a turbulent wake and complex velocity structures.

- **Breakup:** RT instabilities develop as the cloud is accelerated, leading to the fragmentation of the cloud into smaller cloudlets. While not fully captured in the presented simulation time, the onset of fragmentation is suggested in the final panel of Figure 3.1, where the cloud begins to lose its cohesive structure.

The simulation evolution is sensitive to the initial conditions in the interactions, specifically with regard to the size of the cloud and the sharpness of its edges or geometry. The sensitivity of cloud evolution to its initial geometries justifies the need for including more models with other cloud geometries. This would require some experimentation with a greater variety of cloud shapes, such as clouds with smoothed edges similar to the one included in our study, as well as more complex configurations like cylindrical or turbulent clouds. Exploring different morphologies, would help to fully understand how the initial cloud morphology affects the breaking-up of clouds and their subsequent evolution.

3.2 The role of cloud morphology

Our simulations demonstrate the significant impact of initial cloud morphology on the subsequent evolution of interstellar clouds. This is similar with the findings of previous studies, such as those by Goldsmith & Pittard (2019[45]), which highlight the importance of initial conditions in shaping the gravitational collapse process induced by shocks.

In our models, we observe four distinct stages of evolution that appear to be universal across all initial configurations. However, we also observe qualitative differences in the evolution of clouds with different initial morphologies (see Figure 3.3). Clouds with sharp edges (sph-sharp10, sph-sharp5) initially exhibit a uniform density distribution, whereas the smooth cloud (sph-smooth10) starts with a centrally concentrated density profile that smooths towards the edges. As the simulations progress, all cloud models develop complex, filamentary density structures, but the sharp-edged cloud, sph-sharp5, shows a greater tendency for early fragmentation, breaking up into smaller clumps earlier in the evolution compared to the smooth cloud.

One of the most striking differences observed when reducing the initial cloud radius is the effect of time scaling. Indeed, reducing the initial cloud radius (from 10 pc to 5 pc) leads to faster disruption and earlier fragmentation. In essence, the same evolutionary stages occur in all models, but the timescale over which they unfold is significantly shorter for clouds with smaller radii.

Figure 3.4 presents the temporal evolution of six diagnostic parameters for the three distinct cloud models (smooth_{10}, sharp_{10}, sharp_{5}) under the influence of a supersonic wind. The top panels display the time-dependent effective radii of the clouds in both the X (panel a) and Y (panel b) directions. The middle panels track the vertical displacement of the center of mass of the clouds (panel c), and the corresponding mass-weighted velocity in the Y direction (panel d). Finally, the bottom panels reveal the evolution of the mixing fraction (panel e), a measure of mixing fraction, and the velocity dispersion in the Y direction (panel f), an indicator of turbulent motions within the cloud. Below, we discuss some important results:

- **On cloud morphology**: First, we discuss the effects of the morphology of the cloud in panels a) and b) of figure 3.4. Interestingly, the effective initial radius of the smooth-edged cloud (smooth_{10}) starts at 5.8pc, a value at which the density is 0.995 ρ_c, highlighting that the initial effective radius calculation is influenced by the density profile of the cloud defined by Equation 2.6. This contrasts with sharp-edged clouds (sharp_{10} and sharp_{5}), which begin with effective radii of their actual initial radii of 10 pc and 5pc, respectively. As expected, the cloud radius in the Y-direction (aligned with the wind) is consistently larger than in the X-direction for all models, a consequence of the wind predominantly vertical impact, and the constraining effect of the bow shock in the X-direction.

(a) sph-sharp$_{10}$

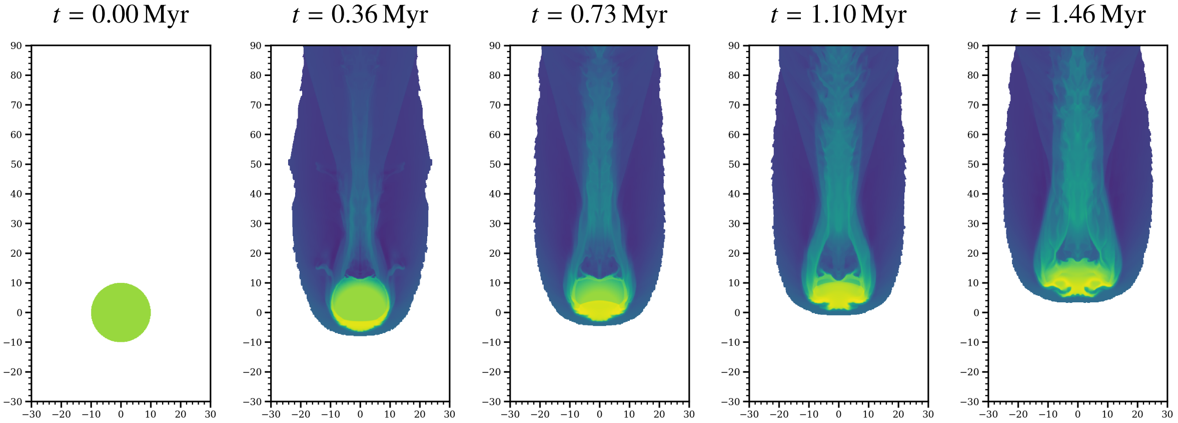

(b) sph-sharp$_5$

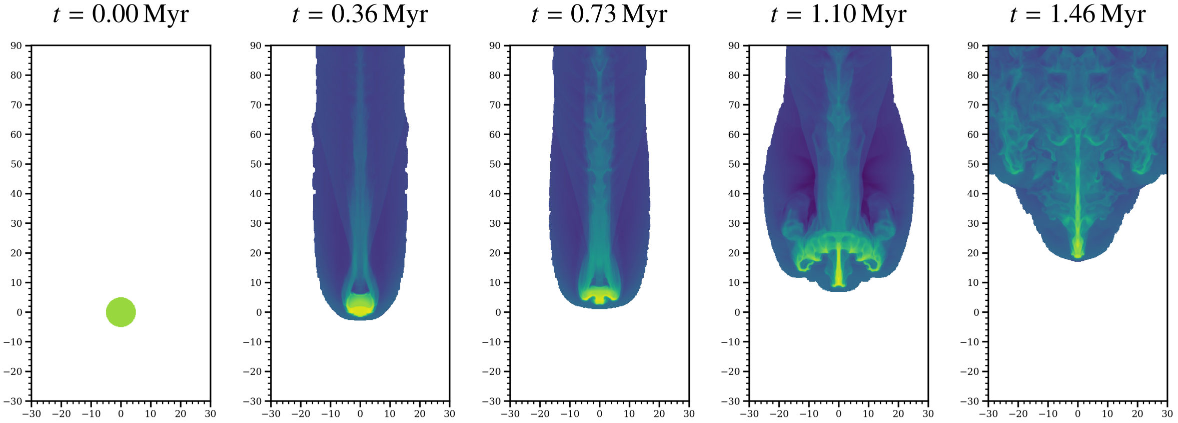

(c) sph-smooth$_{10}$

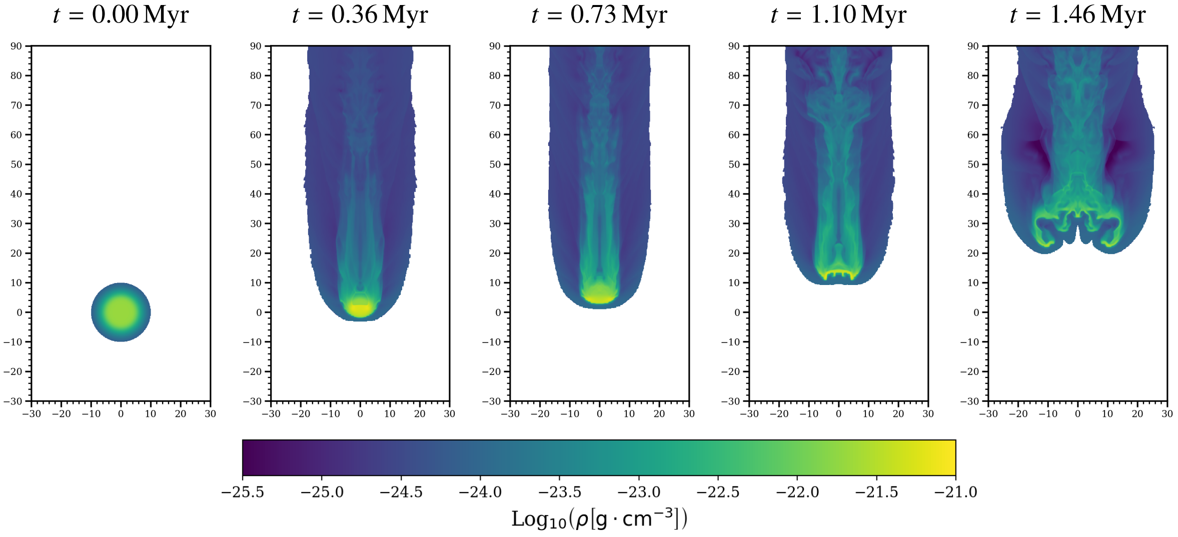

Figure 3.3: 2D slices at $z = 0$pc, showing the evolution of the logarithm of the density for cloud material in the three cloud models, (a), (b), (c). The evolution is shown in 5 different physical times: $t = 0.00, 0.36, 0.73, 1.10$ and 1.46 Myr. This figure highlights the distinct morphological evolution of clouds with different initial conditions as they interact with a wind.

- As the simulations progress, all three clouds experience an initial reduction in their effective radii due to the compressive effects of the wind and the stripping of outer layers. This reduction is more significant in the smooth-edged cloud, likely due to its lower density at the edges. Furthermore, the initial radius of clouds significantly influences the timescale of its evolution. The smaller cloud (sharp$_5$) experiences more rapid changes in its morphology and kinematics than the larger clouds. This is evident in the faster increase in effective radii. This accelerated evolution can be attributed to the smaller lower inertia of the cloud, making it more susceptible to the disruptive forces of the wind and leading to a faster expansion.

- **On cloud kinematics**: The kinematics of the cloud models, as illustrated in panels c) and d) of Figure 3.4, exhibit distinct differences in their motion and acceleration under the influence of the wind. The displacement of the center of mass in the Y-direction (Figure 3.4 c) consistently demonstrates an upward acceleration for all three clouds, along the direction of the wind. In particular, the smaller cloud (sharp$_5$) experiences a faster acceleration (because it is less massive) and achieves a higher final displacement compared to the larger clouds. This disparity in acceleration and displacement is further accentuated in the mass-weighted velocity profiles (Figure 3.4 d).

- The sharp$_5$ model attains a significantly higher velocity than the other two, while the sharp$_{10}$ cloud, exhibits the slowest acceleration and the lowest final velocity. The observed differences in the magnitude and timescale of velocity evolution can then be attributed to variations in cloud size, inertia, and the efficiency of momentum coupling between the wind and the cloud material. Despite these variations, all three velocity profiles share a common shape: an initial rapid increase followed by a gradual leveling off. This similarity suggests a shared underlying mechanism for momentum transfer from the wind to the cloud, regardless of the initial morphology.

- **On cloud turbulence**: Then, we discuss the emergence of turbulence, with the panels e) and f) of Figure 3.4. The mixing fraction (Figure 3.4 e) quantifies the degree of mixing, due to turbulence, between the cloud material and the surrounding wind. All three models exhibit a steady increase in mixing over time, indicating the progressive entrainment of ambient gas into the cloud and the dispersal of cloud material into the wind. Notably, the sharp$_5$ cloud experiences the most rapid increase in mixing, followed by the smooth$_{10}$ cloud, and then the sharp$_{10}$ cloud.

- The rapid increase in mixing observed for the sharp$_5$ cloud can be attributed to its swift disruption and fragmentation, exposing a larger surface area to the wind and facilitating the entrainment of ambient gas, and the onset of disruptive KH instabilities. In contrast, when comparing the smooth$_{10}$ and sharp$_{10}$ clouds, the former exhibits a faster overall mixing rate, likely due to the absence of well-defined edges. The smooth density profile of the smooth$_{10}$ cloud allows the wind to penetrate and mix more readily with the outer layers, gradually eroding the cloud from the outside in and exposing the core to further mixing. Conversely, the sharp$_{10}$ cloud, with its distinct density gradients, initially resists mixing at the edges, but as the wind-driven turbulence intensifies, the core is eventually disrupted and mixed with the surrounding medium.

- The velocity dispersion (Figure 3.4f) provides a measure of the turbulent motions within the cloud. In all models, the velocity dispersion initially increases rapidly, reflecting the generation of turbulence due to the wind-cloud interaction. Interestingly, the smooth$_{10}$ cloud exhibits the highest initial velocity dispersion, followed by sharp$_5$ and then sharp$_{10}$. This result might be attributed to the more centrally concentrated density profile of the smooth cloud, which could lead to a more efficient transfer of kinetic energy from the wind to internal motions within the cloud in the early stages of the interaction.

- However, the rate of increase and the overall magnitude of the velocity dispersion differ among the models over time. Notably, the velocity dispersion in all three models plateaus for a period before increasing again. This temporary plateau could be due to a balance between the generation of turbulence by the wind and the dissipation of turbulent energy through shocks and viscous effects. As the simulation progresses and the cloud structure evolves, the balance shifts, leading to a renewed increase in velocity dispersion. The sharp$_5$ cloud ultimately exhibits the highest velocity dispersion, likely due to the formation of stronger shocks and instabilities at its interface with the wind, while the sharp$_{10}$ cloud experiences the lowest level of turbulence.

Our simulations thus pin down the qualitative evolution of the wind-cloud interactions with a diverse initial cloud morphologies. Although the timescales of the related processes differ significantly, the most responsible physical mechanisms—turbulent mixing, stripping, and the formation of internal shocks—seem to be universal for all cloud configurations, indicating the same fundamental interactions are at play.

However, the initial morphology plays a crucial role in modulating the rate at which these processes unfold. The growth timescales of Kelvin-Helmholtz[41] and Rayleigh-Taylor[41] instabilities,

$$t_{\rm KH} \simeq \frac{\chi_{\rm eff}^{1/2}}{k_{\rm KH}\left(v'_{\rm wind} - v'_{\rm cloud}\right)}, \tag{3.1}$$

$$t_{\rm RT} \simeq \frac{1}{[k_{\rm RT}\,(a_{\rm eff})]^{1/2}}, \tag{3.2}$$

which are key drivers of cloud disruption, are directly influenced by the density contrast and acceleration of the cloud. Smaller sizes and smoother densities lead to faster cloud evolution, with accelerated disruption and mixing, ultimately influencing the cloud crushing time ($t_{\rm cc}$). This underscores the crucial role of cloud geometry in determining the evolutionary trajectory and ultimate fate of clouds in the presence of stellar wind.

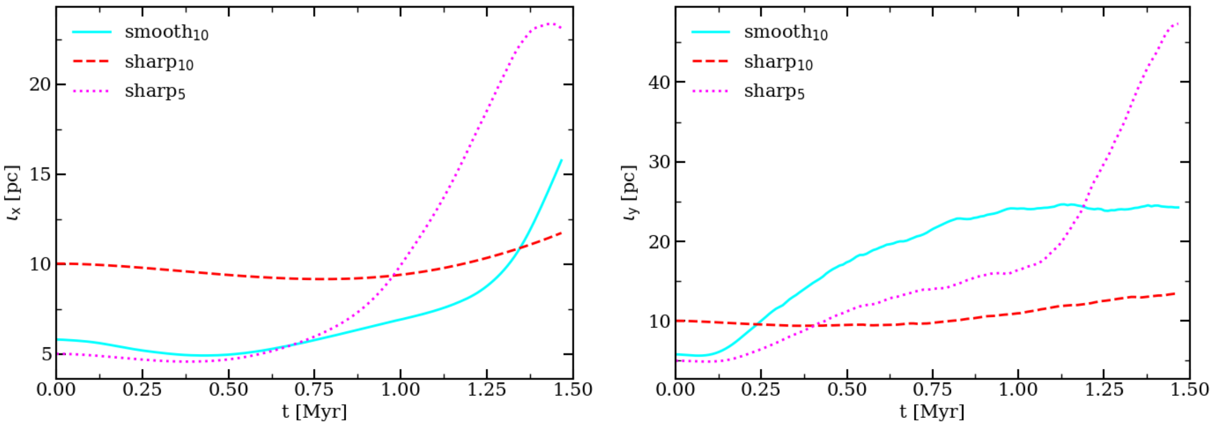

a) Effective cloud radius in X

b) Effective cloud radius in Y

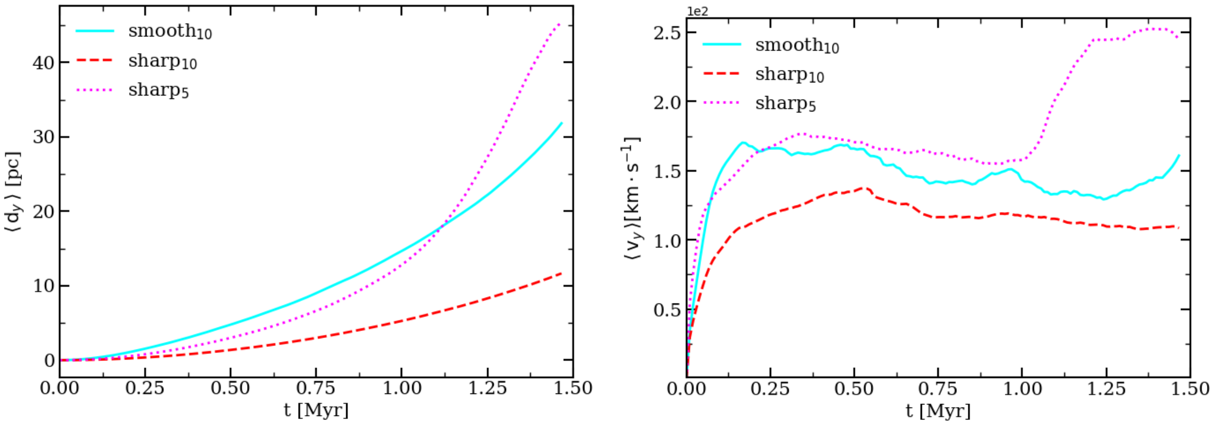

c) Cloud center of mass in Y

d) Cloud velocity in Y

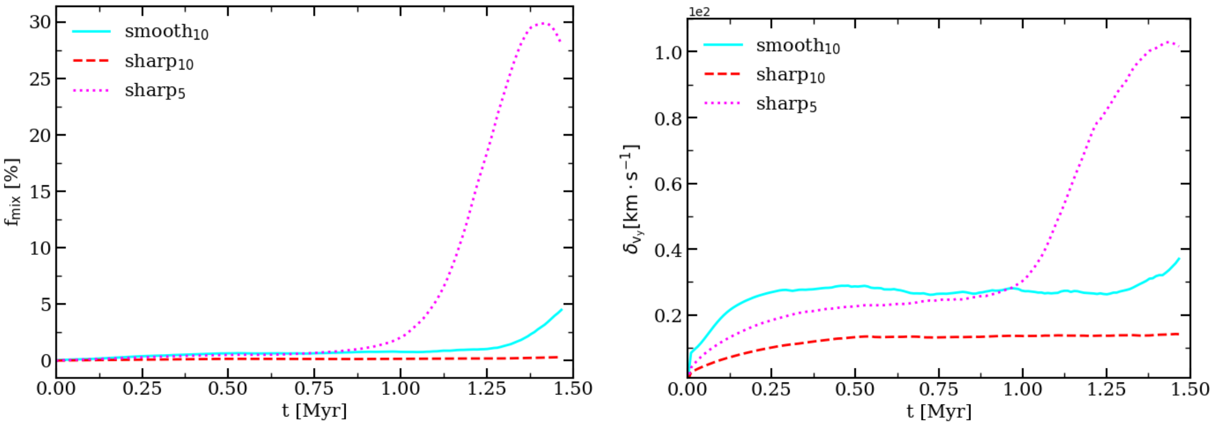

e) Mixing fraction

f) Velocity dispersion in Y

Figure 3.4: Evolution of several cloud diagnostics for the three cloud models (smooth$_{10}$, sharp$_{10}$, sharp$_5$). Panels show: (a, b) effective cloud radii in X and Y directions, (c) center of mass displacement in Y, (d) mass-weighted velocity in Y, (e) mixing fraction, and (f) velocity dispersion in Y. This figure demonstrates the significant impact of initial cloud morphology on the dynamical and turbulent evolution of clouds in a wind-driven environment

3.3 Shocks in wind-cloud models

3.3.1 Searching for convergent flows:

As described in Section 2.2.2, our shock-finding routine uses both velocity divergence and pressure gradient information to identify shock cells. First we analyze the velocity divergence. Figure 3.5 illustrates the temporal evolution of the velocity divergence field for our three cloud models as they interact with the wind. The divergence field serves as a crucial diagnostic tool for identifying regions of flow convergence and divergence, which are indicative of shock formation and flow propagation, respectively.

Initially, all three models exhibit a relatively uniform velocity field with minimal divergence, aside from a slight convergence observed at the leading edge where the wind impacts the cloud, triggering the emergence of the internal cloud shock. As the simulations progress, the patterns of divergence increase in complexity, reflecting the building up of shocks, instabilities, and turbulent mixing. The high values of divergence in all the models show strong regions of diverging flow behind the clouds, these are due to the stripping action by the wind, indicative that the cloud material has been expanded and dispersed. Hence, it displays more extended and turbulent behavior, with a few regions of strong divergence in comparison to the large clouds. This is further supporting the idea that a small cloud becomes strongly disturbed and torn apart by the wind, yielding more complexity and chaos in the wake.

We also observe prominent **bow shocks** forming at the leading edge of each cloud, characterized by strong convergent flows (negative divergence). The area behind the cloud is mostly populated by a network of discontinuities caused by the RT instabilities. Within the clouds, we also observe strong internal convergent flows propagating through the denser regions and oblique flows forming at the edges of the tails. These strong convergent flows are potential shock formation sites that serve as initial shock cell candidates, which are then further analyzed using pressure data to confirm the presence of shocks.

3.3.2 Searching for large pressure gradients:

Figure 3.6 shows the time evolution of pressure gradient magnitude for three cloud models. Pressure gradient is one of the most indicative quantities showing the existence and strength of the shock, since shocks are known for sudden changes in pressure within very short distances. For all models, at the beginning there are almost no pressure gradients. At those places where the wind encounters the clouds, strong pressure gradients develop very rapidly. Most significantly, at the leading edge of each cloud, it indicates the formation of a bow shock in which supersonic wind will bring about a sudden deceleration and compression as it encounters enhanced density material in the cloud. We see sudden pressure changes in the clouds, especially in their inner parts. These transmitted pressure differences, due to the passage of the bow shock into the cloud, then become localized high-pressure gradient regions indicative of internal shocks. As the simulation progresses, the pressure gradient patterns become more complex and less organized, reflecting the increasing dominance of turbulent mixing over the initial planar shock-driven dynamics. For instance, the bow shock for both the smooth_{10} and the sharp_5 clouds flattens with time as the clouds become progressively disrupted and their distinct boundaries erode.

(a) sph-sharp$_{10}$

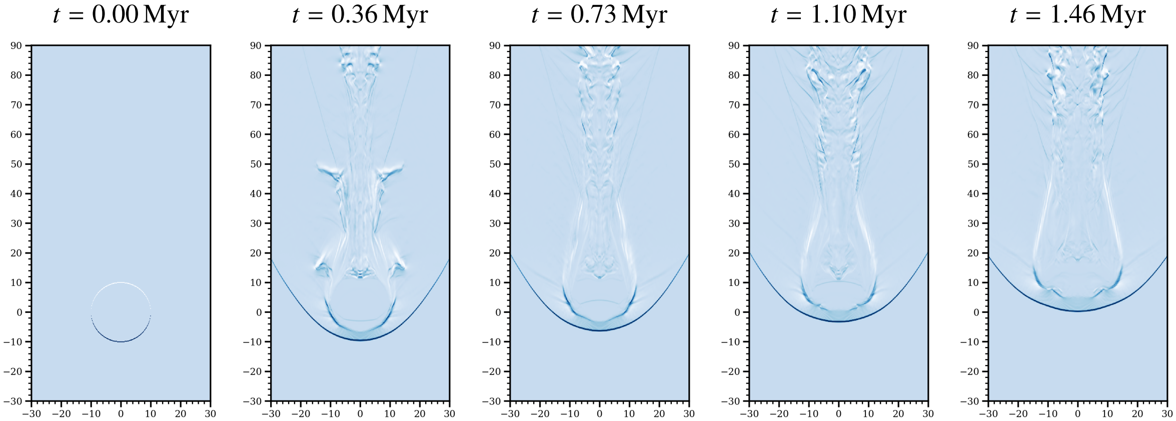

(b) sph-sharp$_5$

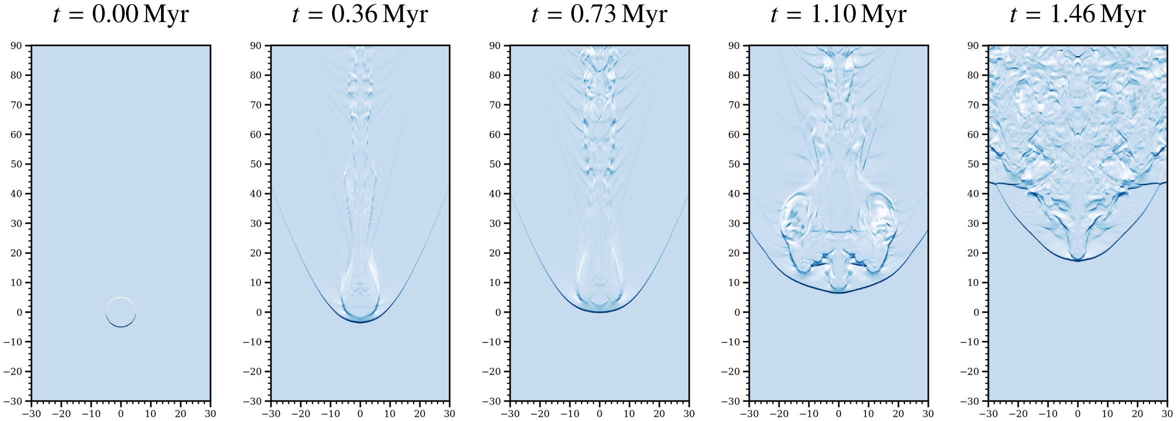

(c) sph-smooth$_{10}$

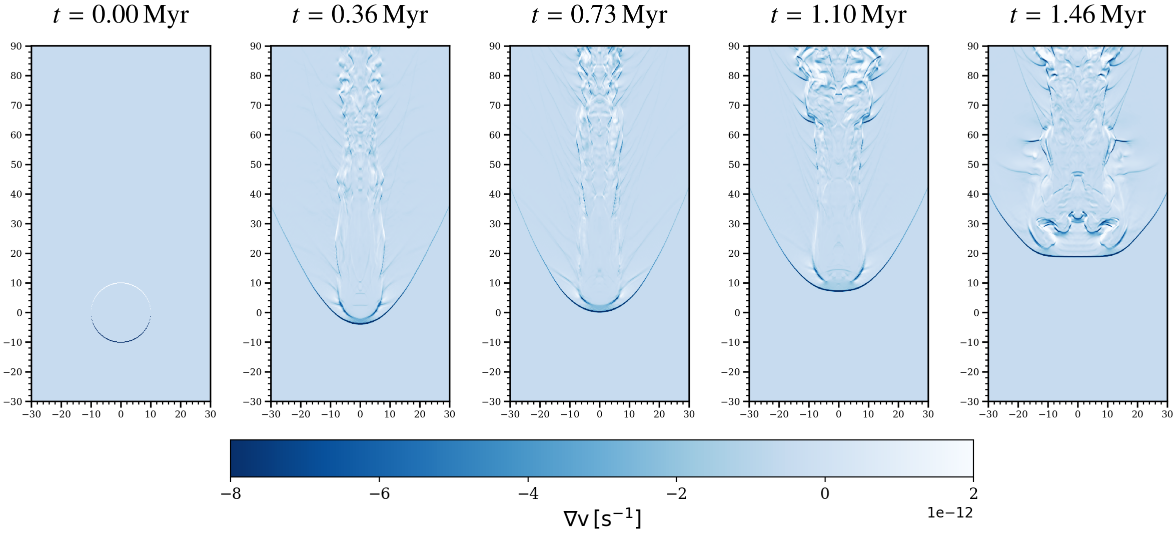

Figure 3.5: 2D slices at $z = 0$pc, showing the evolution of the velocity divergence in the the three cloud models, (a), (b), (c). The evolution is shown in 5 different physical times: $t = 0.00, 0.36, 0.73, 1.10$ and 1.46 Myr. Darker colors indicate convergent flow, while lighter colors represent divergent flow. Shock candidates are primarily associated with regions of strong convergence (darker colors).

(a) sph-sharp$_{10}$

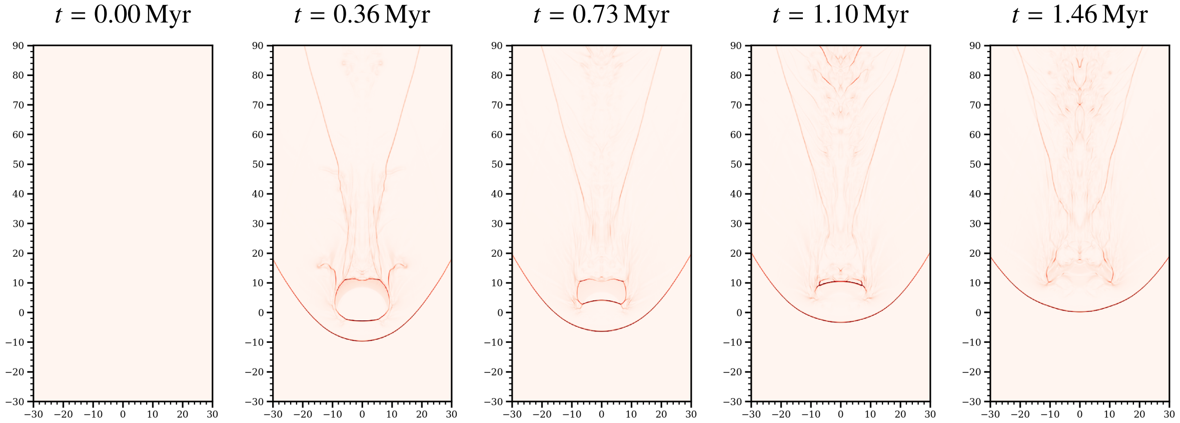

(b) sph-sharp$_5$

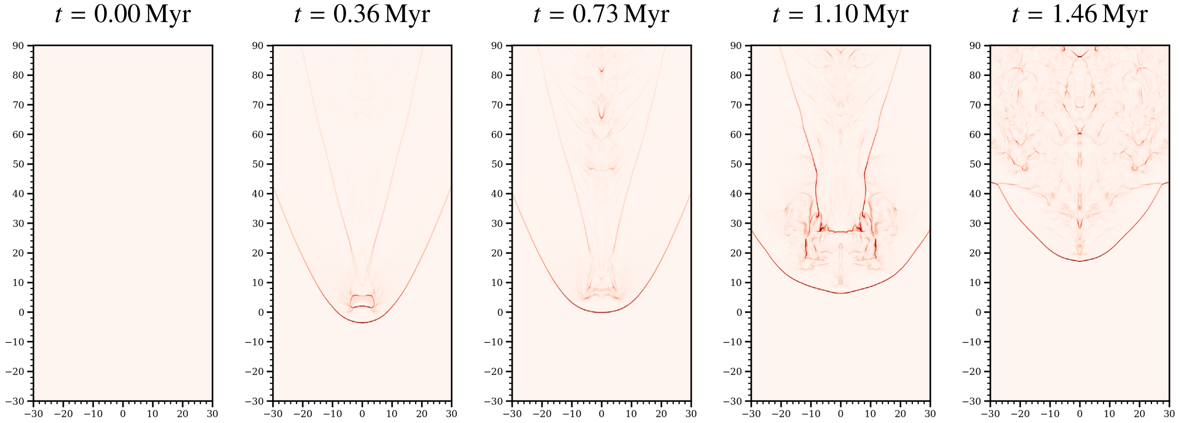

(c) sph-smooth$_{10}$

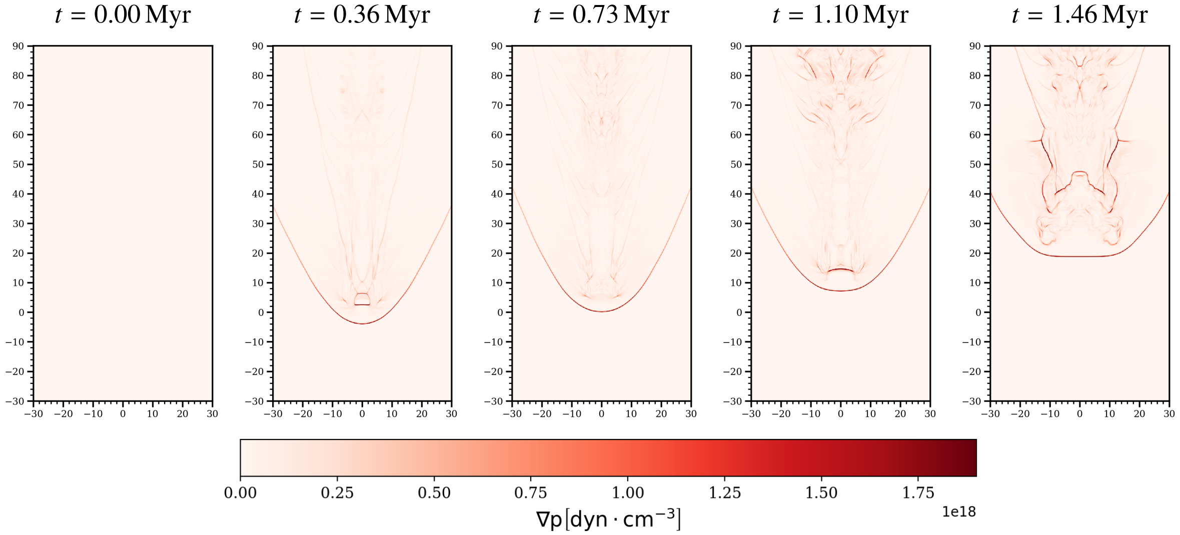

Figure 3.6: 2D slices at $z = 0$pc, showing the evolution of the pressure gradient in the the three cloud models, (a), (b), (c). The evolution is shown in 5 different physical times: $t = 0.00, 0.36, 0.73, 1.10$ and 1.46 Myr.

3.3.3 Shock population and typical shock Mach numbers:

Figure 3.8 displays the spatial distribution and intensity of shocks within the three cloud models at various stages of their interaction with the wind. The Mach number (calculated with Eq 2.5), is used to color-code the shock cells, providing a visual representation of the shock strengths. Initially (t = 0.00 Myr), the velocity field is relatively uniform, with no shocks present as the wind has not yet encountered the clouds.

Across all three models, the dominant shock structures include the bow shock at the leading edge, the internal shock within the cloud, and a conical shock structure behind the cloud. As the simulation progresses, prominent bow shocks rapidly develop at the leading edge of each cloud, characterized by high Mach numbers ($\mathcal{M} > 4$).

Within the clouds, internal shocks emerge as the bow shock propagates through the denser regions. These internal shocks are also characterized by high Mach numbers, although generally lower than those of the bow shocks. Notably, the internal shock in the sharp$_{10}$ model maintains a clear and consistent presence throughout all time steps, a feature not observed in the sharp$_5$ and smmoth$_{10}$ models where the cloud is disrupted after the third snapshot (t = 0.73 Myr).

The sharp$_{10}$ model is also observed to undergo changes in concavity, ranging from an initial concave outward to a later concave inward curve for the evolution of the internal shock. In that regard, the morphological evolution of the shock front is likely to be affected by the complex interplay of gas dynamics, pressure gradients, and the evolving density structure of the cloud. As the simulation reaches the later stages, the overall shock strengths grow weaker because the clouds are highly disrupted and the density contrast is much reduced. There are, however, localized regions with high Mach numbers indicative of strong shocks within the turbulent flow that do continue to exist. The exact extents and strengths of these shocks vary between the models, as might reasonably be expected from the role of initial cloud morphology in driving shock dynamics.

3.3.4 Histograms of shock Mach numbers:

To complement the analysis of individual shock structures, we now investigate the overall shock population within the wind-cloud system. Figure 3.7 presents the temporal evolution of Mach number histograms for the entire computational domain and for the cloud material alone. These histograms provide valuable insights into how the distribution and strength of shocks change over time for each of the three cloud models.

Across all models and times, a prominent peak near $\mathcal{M} = 1$ is evident, indicating a significant presence of transonic flows within the undisturbed cloud and ambient medium. While the majority of the distribution lies within the supersonic regime ($\mathcal{M} > 1$), as expected in wind-cloud interactions, the presence of subsonic flows highlights that not all convergent regions identified in the velocity divergence maps (Figure 3.5) correspond to shocks. Our shock-finding algorithm, which incorporates both velocity divergence and pressure gradient information, helps to distinguish true shocks from other convergent flows.

Another notable characteristic of the distributions is a plateau or resistance region around $\mathcal{M} \approx 4$, suggesting that it may represent a quasi-equilibrium state in the shock evolution process. This is consistent with the fact that the wind was set with a $\mathcal{M}_w = 4$ (see 2.4.1).

Subtle variations are observable between the three cloud models. The sharp$_5$ and smooth$_{10}$ models exhibit a resurgence of high-Mach shocks in the later stages of the simulation, which may be attributed to the formation of structures resembling de Laval nozzles. As the clouds fragment due to Rayleigh-Taylor instabilities, the wind can be channeled and accelerated through the gaps between the cloudlets, creating conditions similar to those in a de Laval nozzle. Then this picture is consistent with findings of F. Teuttloff thesis[37].

(a) sph-sharp$_{10}$

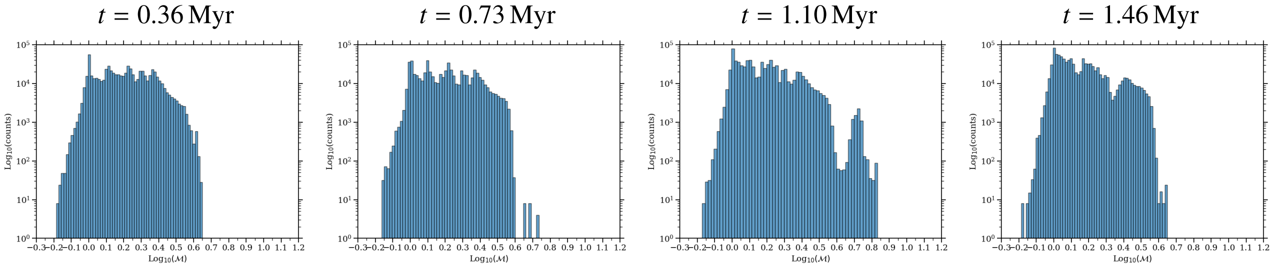
t = 0.36 Myr t = 0.73 Myr t = 1.10 Myr t = 1.46 Myr

(b) sph-sharp$_5$

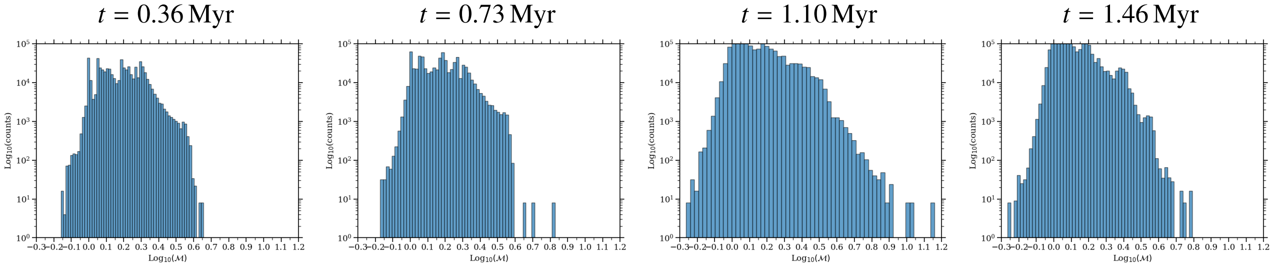
t = 0.36 Myr t = 0.73 Myr t = 1.10 Myr t = 1.46 Myr

(c) sph-smooth$_{10}$

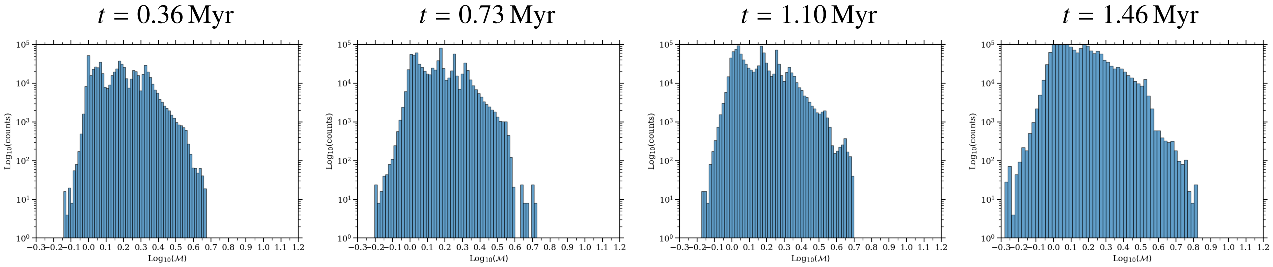
t = 0.36 Myr t = 0.73 Myr t = 1.10 Myr t = 1.46 Myr

Figure 3.7: Mach number histograms for all computational domain of the three cloud models, (a), (b), (c). The evolution is shown in 4 different physical times: $t = 0.36, 0.73, 1.10$ and 1.46 Myr. This figure shows the temporal evolution of shock intensities in wind-cloud interactions, revealing a small number of subsonic cells, an initial plateau at $\mathcal{M} \approx 4$ and a progressive increase in shock intensity due to turbulence.

(a) sph-sharp$_{10}$

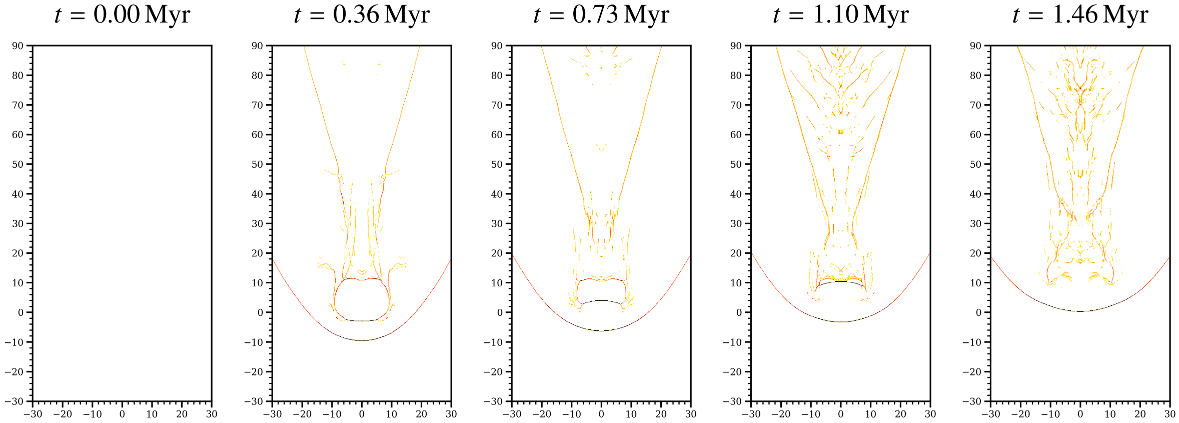

(b) sph-sharp$_5$

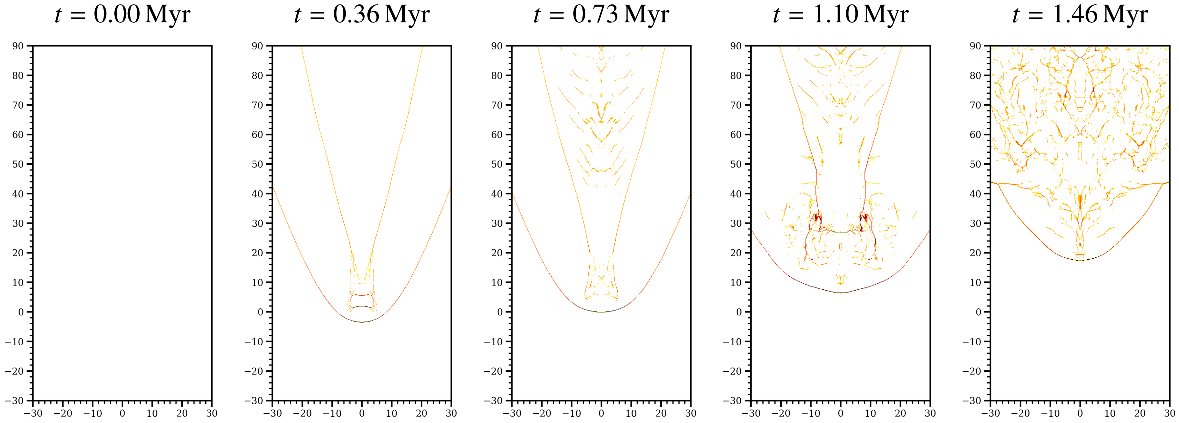

(c) sph-smooth$_{10}$

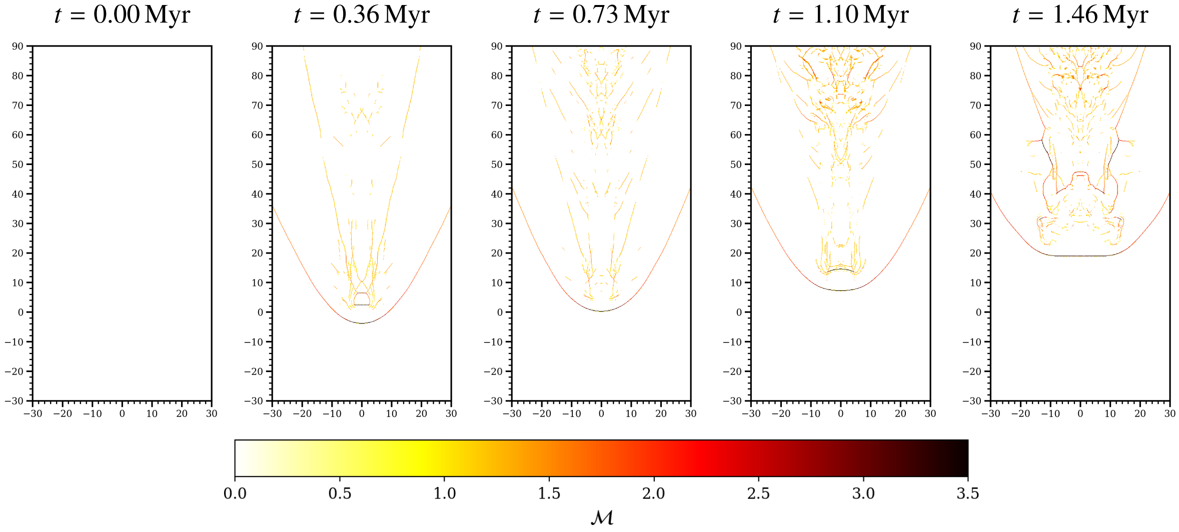

Figure 3.8: 2D slices at z = 0pc, showing the evolution of the shock cells in the the three cloud models, (a), (b), (c). The evolution is shown in 5 different physical times: $t = 0.00, 0.36, 0.73, 1.10$ and 1.46 Myr. This figure visualizes the formation, propagation, and morphological changes of shocks within the clouds as they interact with the wind.

3.4 On cloud-crushing times from the internal shock viewpoint

3.4.1 Analytical approach

Having successfully identified the shock cells in the three simulations, we now proceed to estimate the cloud destruction times-scales, known as cloud crushing time (t_{cc}). To this end, we will employ the analytical equations proposed by Klein et al. (1994) (Equation 1.1) and Jones et al. (1996) (Equation 1.3), which offer a first approximation to this crucial parameter. In both formulations, t_{cc} depends on the velocity of the wind and the density contrast between the cloud and the surrounding medium. Given that the wind magnitude is constant in our three simulations, it is evident that the t_{cc} for the sharp$_5$ cloud (with an initial radius of 5 pc) will be smaller than that of the sharp$_{10}$ cloud (with an initial radius of 10 pc). However, estimating the t_{cc} for the smooth$_{10}$ cloud presents a challenge.

Although its initial radius was set to 10 pc, its effective radius, calculated from the density profile, is only 5.8 pc. For our analytical t_{cc} calculations, we will adopt this effective radius as the relevant cloud size. Furthermore, although the cloud density is not uniform, we will consider the core density as the representative value for our analytical t_{cc} analysis, as this is the region where the internal shock predominantly propagates.

Therefore, the following table presents the t_{cc} values obtained for each cloud model using both analytical formulations:

Model	$t_{\mathrm{cc,K}}$ (Myr)	$t_{\mathrm{cc,J}}$ (Myr)
sharp$_{10}$	0.598	1.197
sharp$_5$	0.299	0.598
smooth$_{10}$	0.347	0.694

Table 3.1: Cloud crushing times (t_{cc}) for the three cloud models, calculated using the analytical expressions by Klein et al. (1994) and Jones et al. (1996).

It is important to remember that these are rough estimates derived from simplified assumptions. Hence, we need to get more accurate and realistic t_{cc} values following the dynamic evolution of clouds and shocks, which we have done by performing shock-tracking technique described in Section 2.2.3 to numerically obtain the t_{cc} for each cloud model. Using this approach, we follow how an internal shock front propagates throughout a cloud and define an instant when the internal shock front catches up to the trailing edge of the cloud, marking its effective destruction. Figure 3.9 shows the results of this numerical analysis. We plot the time evolution of the internal shock and, in blue, indicate the last cell of the internal shock detected. We can now compare these numerical results with the analytical estimates provided in Table 3.1 to check the validity of simplified assumptions used in analytical models and then draw physically meaningful conclusions about the timescale of cloud disruption.

3.4.2 Numerical approach

First, we show the shock-tracking result maps. In Figure 3.9, the evolution of shock cells, identified using our shock-finding algorithm (which tracks cells with $\mathcal{M} > 3$), aligns well with the internal shock progression across all three simulations. The internal shock morphology exhibits a consistent pattern across the models, initially forming a U-shape due to the spherical geometry of the cloud. This U-shape subsequently flattens as the shock propagates through the cloud. This flattening is attributed to the higher shock velocity at the center of the cloud, compared to the edges. As the simulation progresses, the internal shock concavity reverses, resulting in an inverted U-shape. This phenomenon is captured by our shock-tracking algorithm, which initially identifies the edges of the U-shaped shock as the last detected shock cells. However, as the shock evolves and changes concavity, the algorithm correctly tracks the center of the inverted U-shaped shock front as the last shock cell.

Notably, in the sharp$_5$ and sharp$_{10}$ models, the shock-tracking routine accurately follows the internal shock until its disappearance after $t_{\rm cc}$=1 Myr. However, for the smooth$_{10}$ model, the shock cannot be tracked beyond 0.749 $t_{\rm cc}$, as seen in the last two panels of Figure 3.9. This discrepancy provides a clear initial indication that the analytical $t_{\rm cc}$ does not perfectly align with the simulation results, emphasizing the necessity of a numerical estimation.

To further investigate the discrepancies between the theoretical and observed cloud crushing times, we examine the evolution of the last shock cell detected by our algorithm in relation to the last cell of dense cloud material ($\rho_{0,clo}/2$). Figure 3.9 presents the temporal evolution of these two parameters, providing a direct visualization of the internal motion of the shock through the cloud.

In the figure 3.10 we have the last shock cell (cyan line) and the last dense cloud cell (red dashed line) for each of the three cloud models. The cyan line becomes blurred after a certain point, indicating the region beyond the scope of our analysis, where the cloud has been significantly disrupted. The vertical dashed line marks the numerical cloud crushing time ($t_{\rm cc}$), defined as the moment when the last dense cloud cell is within 98% of the last shock cell, providing a degree of tolerance in our approximation.

The fluctuations shown in the curves, very evident in the sharp$_{10}$ model, are caused by turbulent motions at the edges of the cloud, which are triggered by Rayleigh-Taylor instabilities. They make the boundary of the cloud quite irregular, with oscillations in the position of the last dense cell of the cloud. Another way to do this is to use schemes with smaller numerical dissipation, which would give better mitigating of these fluctuations and hence a smoother shock front evolution. However, such a step will result in poor accuracy in the complex dynamics of wind-cloud interaction.

The transmission of the shock into the cloud not only compresses and heats the gas but also imparts kinetic energy to the cloud material. This energy transfer manifests as an abrupt increase in the position of the last dense cloud cell, as seen in all three models. This sudden acceleration of the cloud material is a direct consequence of the adiabatic nature of the simulations, where the energy of the shock is primarily converted into kinetic energy rather than being radiated away.

(a) sph-sharp$_{10}$

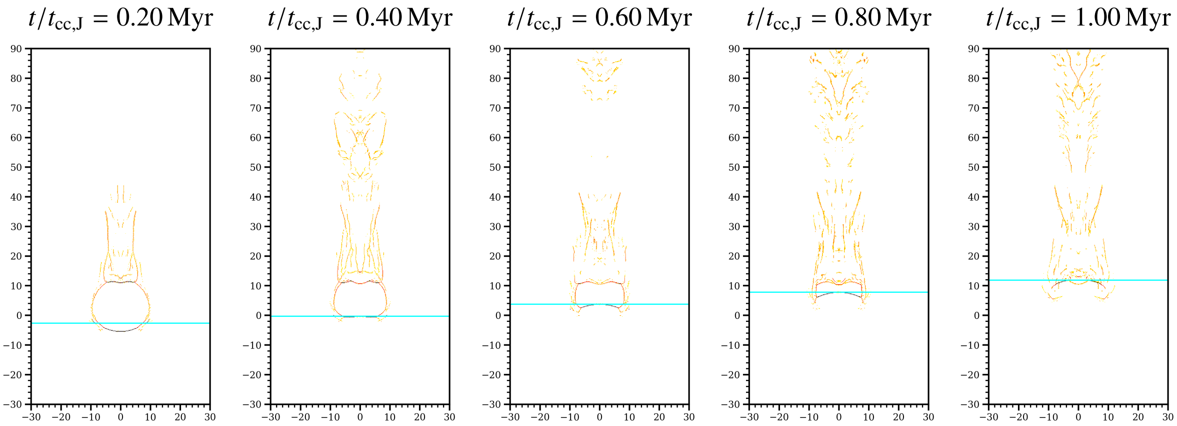

(b) sph-sharp$_5$

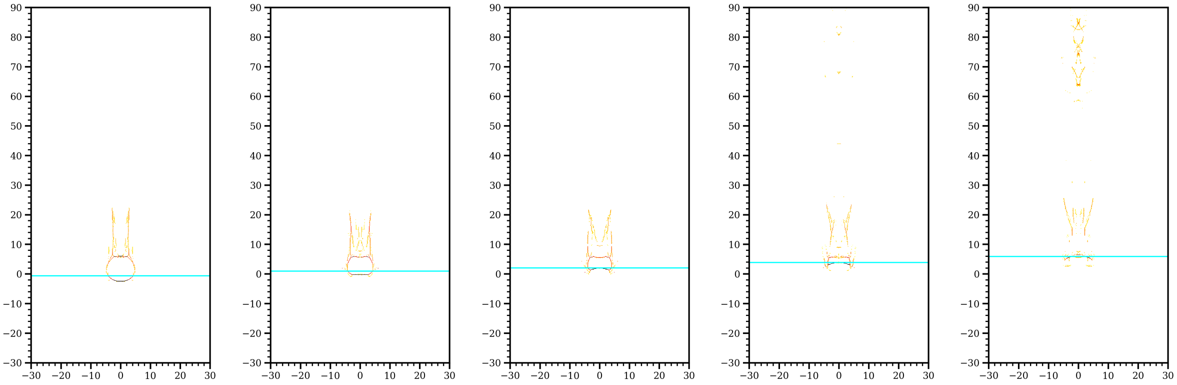

(c) sph-smooth$_{10}$

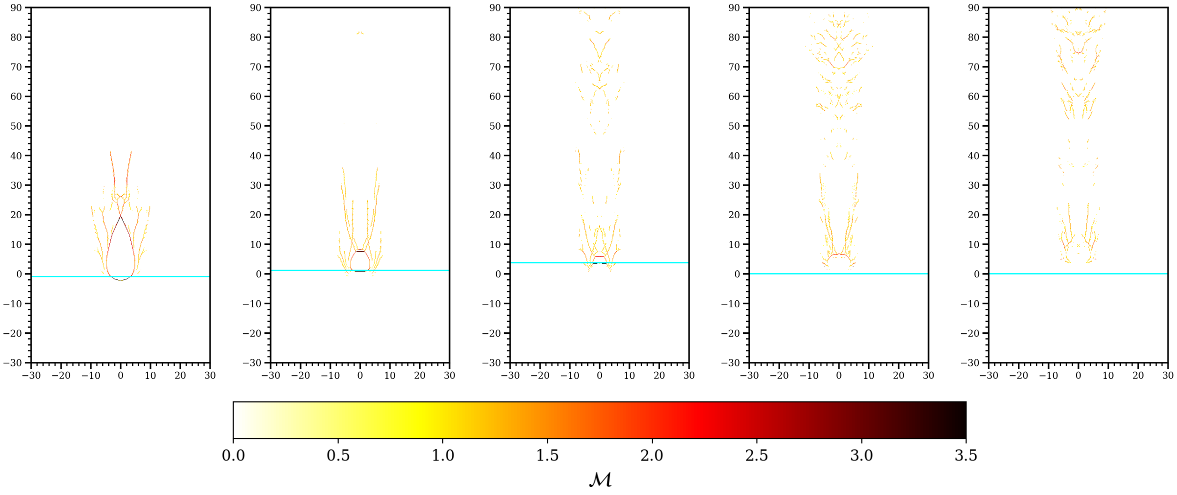

Figure 3.9: 2D slices at $z = 0$pc, showing the evolution of the intern shock cells and the last shock cell detected in the the three cloud models, (a), (b), (c). The evolution is shown in 5 different times: $t = 0.00, 0.36, 0.73, 1.10$ and 1.46 Myr. The blue line indicates the position of the last internal shock cell detected by the shock tracking algorithm.

(a) sph-sharp$_{10}$

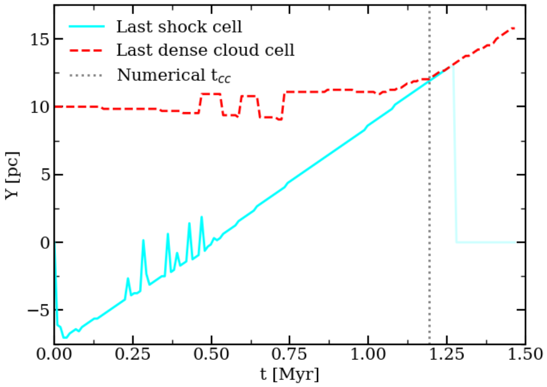

(b) sph-sharp$_5$

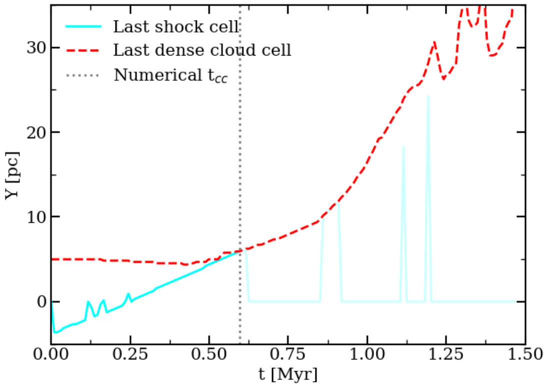

(c) sph-smooth$_{10}$

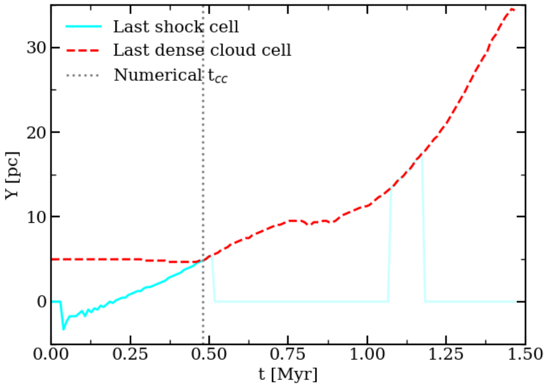

Figure 3.10: Temporal evolution of the last shock cell and last dense cloud of the three models: (a) sph-sharp$_{10}$, (b) sph-sharp$_5$, (c) sph-smooth$_{10}$. In each panel, there are three main elements: the blue line indicates the evolution of the last internal shock cell, becoming transparent after the shock reaches the cloud as it's no longer of interest; the red line shows the evolution of the last dense cloud cell; and the vertical dotted line represents the exact time when the shock reaches the back of the cloud, which is our numerical t_{cc}.

Model	$t_{\mathrm{cc,K}}$ (Myr)	$t_{\mathrm{cc,J}}$ (Myr)	$t_{\mathrm{cc,num}}$ (Myr)	$\epsilon_{\mathrm{r,K}}$ (%)	$\epsilon_{\mathrm{r,J}}$ (%)
sharp_{10}	0.598	1.197	1.193	99.50	0.33
sharp_{5}	0.299	0.598	0.596	99.33	0.33
smooth_{10}	0.347	0.694	0.479	38.04	30.98

Table 3.2: Cloud crushing times (t_{cc}) for the three cloud models, calculated using the analytical expressions by Klein et al. (1994) and Jones et al. (1996), the numerical approximation and the relative errors ϵ_{r} between each analytical expression and the numerical approximation.

The numerical t_{cc} values obtained from Figure 3.9 are presented in Table 3.2, alongside the theoretical estimates from Klein et al. (1994) and Jones et al. (1996). A comparison of these values reveals that the numerical t_{cc} for the sharp_5 and sharp_{10} models agree reasonably well with the theoretical predictions of Jones et al. (1994). However, for the smooth_{10} model, the numerical t_{cc} is shorter than the Jones approximation and larger than the Klein approximation, highlighting the limitations of the analytical approximations in capturing the complex dynamics of non-uniform density clouds.

3.4.3 Redefining the calculation of the cloud-crushing time, t_{cc}

To refine the analytic estimation of the t_{cc}, we explore alternative approaches that account for the non-uniform density distribution within the smooth_{10} cloud. Table 3.4 presents the t_{cc} values obtained using different density averages in the analytical formulations of Jones et al. (1996). We consider two scenarios for the smooth_{10} cloud: using its full initial radius of 10 pc and its effective radius of 5.8 pc. For each radius, we calculate t_{cc} using three different density values: the mean volume-averaged density, the mean mass-weighted average density, and the median density. Additionally, we introduce two novel approaches that involve calculating t_{cc} for each individual cell within the cloud, taking into account the local density and shock properties. This approach provides a distribution of t_{cc} values, offering insights into the spatial variation of the disruption timescale of the cloud.

r_{c}	$t_{\mathrm{cc},[\,\rho_0\,]}$ (Myr)	$t_{\mathrm{cc},\langle\,\rho_0\,\rangle}$ (Myr)	$t_{\mathrm{cc},\tilde{\rho}_0}$ (Myr)	$t_{\mathrm{cc},\bar{\mathrm{t}}_{\mathrm{cc}}}$ (Myr)	$t_{\mathrm{cc},\tilde{\mathrm{t}}_{\mathrm{cc}}}$ (Myr)
10.0	0.457	1.000	0.123	0.298	0.123
5.8	0.132	0.290	0.347	0.347	0.347

Table 3.3: Cloud-crushing time values, considering ten different ways of calculating it.

The t_{cc} values that deviate the most from the numerical estimates are those calculated using the mass-weighted volume average of the initial cloud density, $\langle\,\rho_0\,\rangle$, the median of the cloud-crushing time $\tilde{t}_{\mathrm{cc}}$ distribution and the median of the initial cloud density, $\tilde{\rho}_0$. This discrepancy may be attributed to the non-Gaussian nature of these distributions, as illustrated in Figure 3.11. It looks more like a bimodal distribution.

r_c	$\epsilon_{\mathrm{r},[\rho_0]}$ (%)	$\epsilon_{\mathrm{r},\langle\rho_0\rangle}$ (%)	$\epsilon_{\mathrm{r},\tilde{\rho}_0}$ (%)	$\epsilon_{\mathrm{r},\bar{\mathrm{t}}_{\mathrm{cc}}}$ (%)	$\epsilon_{\mathrm{r},\tilde{\mathrm{t}}_{\mathrm{cc}}}$ (%)
10.0	4.52	108.89	74.15	37.78	74.15
5.8	72.31	39.42	27.51	27.51	27.51

Table 3.4: Relative errors of the cloud-crushing time values from numerical estimation, considering ten different ways of calculating it.

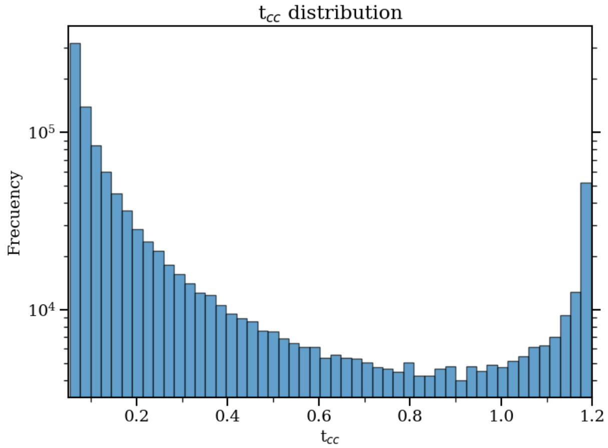

Figure 3.11: Histogram of the distribution of t_{cc} values at t = 0.00 Myr of smooth$_{10}$ cloud. The graph shows a U-shaped distribution, where the right side corresponds to the denser center of the cloud, and the left side represents the edges of the cloud where the density is lower.

On the other hand, the value that most closely aligns with the numerical estimation is obtained by considering the volume-averaged initial cloud density ($[\rho_0]$), resulting in a different density contrast (χ_{eff}). Therefore, a better estimate of cloud disruption time-scales is a variant of Jones's proposal:

$$t_{\mathrm{cc}} = \chi_{\mathrm{eff}}^{1/2} \frac{2 r_{\mathrm{c}}}{\mathcal{M}_{\mathrm{w}} c_{\mathrm{w}}}, \tag{3.3}$$

where χ_{eff} is the density contrast between the cloud and the inter-cloud medium, defined as:

$$\chi_{\mathrm{eff}} \equiv \frac{[\rho_0]}{\rho_{i0}}. \tag{3.4}$$

3.5 Numerical Convergence

To ensure the reliability of our simulations, we performed a numerical convergence test. The idea behind this is to vary the resolution (given by the number of cells per cloud radius) of a specific model to observe qualitative and

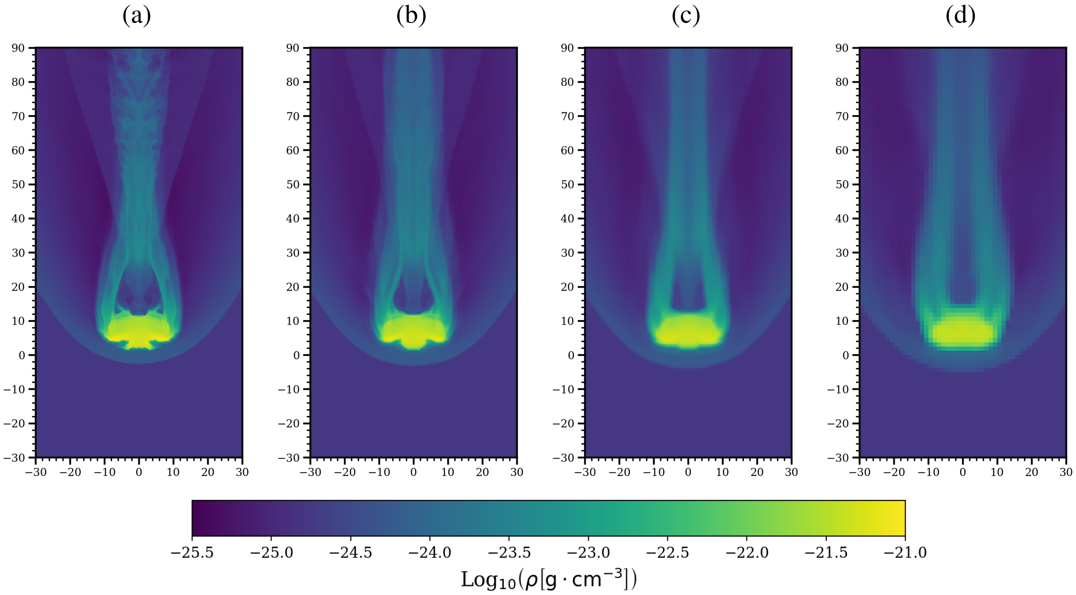

Figure 3.12: 2D density slices on the XY plane at $z = 0$ pc and $t_{cc} = 1$ Myr for the sharp$_{10}$ model at different resolutions. Panel (a) shows a model with a resolution of R$_{64}$. Panel (b) has R$_{32}$, panel (c) has R$_{16}$, and panel (d) has R$_{8}$. This figure illustrates the same model at the same time with different resolutions to show the qualitative differences between them.

quantitative differences. This is of vital importance, as cloud disruption is governed by RT and KH instabilities, which grow at different length scales. For this analysis, we conducted three additional simulations of the spherical model with sharp edges and a 10 pc radius, using the same initial and boundary conditions, varying only the resolution. We sequentially increased the resolution, doubling it from R$_{8}$ to R$_{64}$.

Let us first examine the qualitative aspect in Figure 3.12. This figure shows an XY slice at time $t_{cc} = 1$ Myr. Two key differences can be observed. As resolution increases, the tail of the cloud becomes less diffuse. Then, at higher resolution simulations better capture the turbulence in the tail region. The leading edge of the cloud shows clear differences between models. A characteristic 'W' shape becomes more pronounced in higher-resolution simulations, particularly in R$_{64}$, where more bubbles penetrate the cloud, similar to what was observed by Jones et al, 1996[30]. This feature indicates that RT instabilities are more effectively captured at higher resolutions as smaller eddies become resolved.

Besides the above discussed qualitative differences in evolution, we need to analyse the quantitative differences in the evolution of these four models. To do this, we performed a time evolution diagnostic plotted in Figure 3.13. The figure contains four panels, each for a different parameter: a) Cloud center of mass in the Y direction, b) Cloud velocity in the Y direction, c) Effective cloud radius in the X direction, and d) Velocity dispersion in the Y direction.

For all parameters, the R_8 simulation overestimates the values, proving the limitations of low-resolution models in capturing the dynamics of the cloud. We found that the R_{32} simulation gives the closest agreement with the highest resolution R_{64} model, and thus it may offer some reasonable compromise between computational efficiency and accuracy for some applications. It should, however, be noted that even R_{32} tends to overestimate a few parameters, such as the vertical velocity of the cloud in Y direction and the velocity dispersion.

In general, the R_{64} simulations converge to consistent values and demonstrate stability over time. This convergence is evident across the multiple diagnostics presented. While higher resolutions might capture tail turbulence in more detail, this level of detail on that certain region is beyond the scope of the current study. Therefore, we conclude that a resolution of R_{64} is sufficiently adequate for our purposes, which is why it was the resolution chosen for the previous parts.

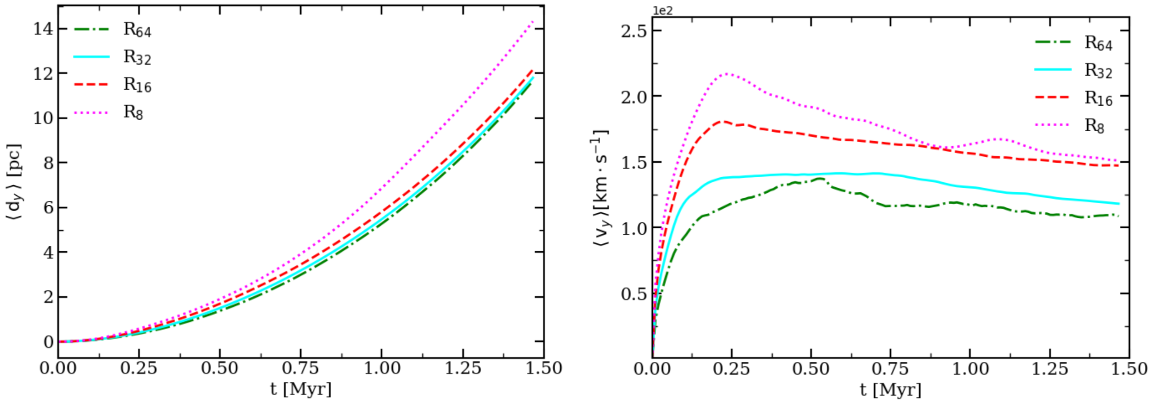
a) Cloud center of mass in Y

b) Cloud velocity in Y

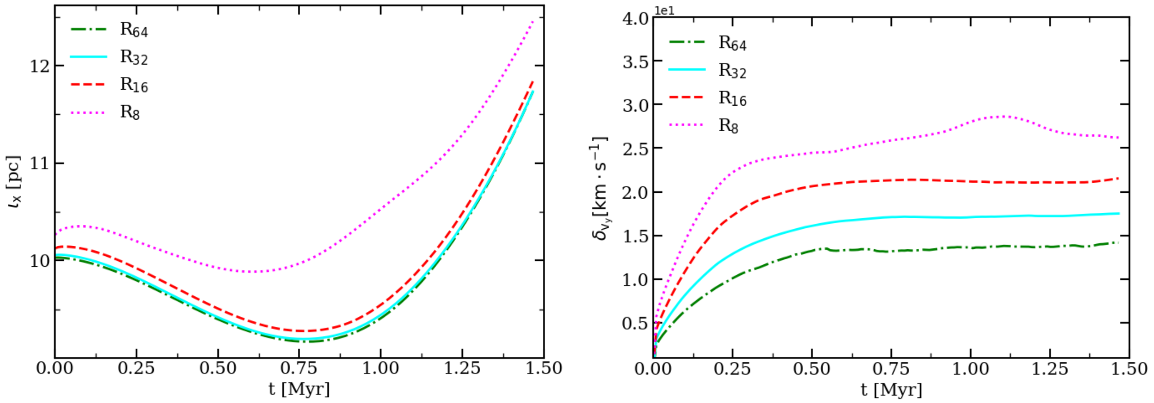
c) Effective cloud radius in X

d) Velocity dispersion in Y

Figure 3.13: Evolution of several cloud diagnostics for the sharp$_{10}$ model with different resolution. Panels show: a) cloud center of mass in Y, b) cloud velocity in Y, c) effective cloud radius in X, d) Velocity dispersion in Y. This figure demonstrates the significant impact of the resolution on the evolution of several cloud diagnostics.

Chapter 4

Conclusions & Outlook

Motivated by the wide range of cloud crushing timescales ($t_{\rm cc}$) reported in previous numerical and theoretical studies of interstellar wind-cloud interactions, we investigated the impact of cloud morphology and density distribution on the evolution of wind-cloud systems, the resulting shock structures, and the timescales governing cloud disruption. We performed 3D HD simulations using the PLUTO code on high-performance computing facilities, to model the interaction of a supersonic wind with initially spherical clouds of varying sizes and edge profiles. To analyze the complex, multi-phase gas resulting from these interactions, we developed our Python-based, shock-tracking into a module, and enhanced our shock-finding routine to numerically characterize the cloud-crushing time. Our main conclusions are the following: (Nittmann et al. 1982[44]; Klein et al. 1994[2]; Banda-Barragán et al. 2016[16])

- High-resolution wind-cloud simulations capture the complex morphological evolution of interstellar clouds. The formation of filaments, the appearance of instabilities, and the fragmentation of ISM and CGM clouds are dynamic processes that highlight the importance of numerical simulations for understanding wind-cloud interactions and the ISM and CGM environments that they occur within.
- Our simulations confirm that the four-stage disruption process (compression, stripping, expansion, and breakup) provides a consistent view for understanding wind-cloud interactions, regardless of the specific cloud geometry. While the timescale and details of each stage may vary depending on the initial conditions, the overall sequence of events appears to be universal, in agreement with studies by Nittmann et al. 1982[44], Klein et al. 1994[2], Banda-Barragán et al. 2016[16].
- Our 3D wind-cloud simulations show that the initial cloud morphology significantly influences the evolution of wind-cloud systems, affecting the rate of morphological changes, kinematics and turbulence. These findings underscore the importance of considering detailed cloud geometry in numerical simulations.
- The underlying physical processes driving wind-cloud interactions are universal across different cloud morphologies. However, initial geometry acts as a modulator, influencing the rate and intensity of these processes, ultimately impacting the evolutionary trajectory and fate of wind-swept clouds.

- The time evolution of shocks resulting from the interaction of winds and clouds can be pretty complex, depending on the morphology of the cloud at the start. Bow shock at the leading edge, internal shocks within the cloud, and a conical shock structure behind the cloud are the three main observed shock structures in our simulations.

- Analysis of the overall shock population reveals a characteristic Mach number distribution, with a prominent peak near $\mathcal{M} = 1$ (transonic flows) and a plateau around $\mathcal{M} \approx 4$. This suggests the presence of a quasi-equilibrium state in the shock evolution process, consistent with the initial wind Mach number ($\mathcal{M}_{\rm w} = 4$). Additionally, in the later stages of the simulation, there is a resurgence of high-Mach shocks, with typical $\mathcal{M}$ between 3 and 6, attributed to increased turbulence and the formation of structures resembling de Laval nozzles, where the wind is channeled and accelerated through gaps between cloudlets formed by Rayleigh-Taylor instabilities. The latter result is in agreement with work by Teutloff 2021[37].

- The internal shock morphology evolves consistently across all models, starting with a U-shape due to spherical geometry of the cloud, then flattening, and finally inverting into an upstream U-shape. This evolution is accurately captured by our novel shock-tracking algorithm, demonstrating its effectiveness in following the internal shock progression with a Python routine that relies on the Rankine-Hugoniot conditions.

- The numerical estimate of cloud-crushing time shows agreement with analytical predictions for clouds with uniform density distribution, with an error of only 0.33% with respect to the formulation of Jones et al. (1996). However, for the smooth density profile cloud (smooth$_{10}$), the numerical $t_{\rm cc}$ is shorter than analytical predictions, highlighting the limitations of simplified analytical models for non-uniform density clouds.

- A refined analytical approach for estimating $t_{\rm cc}$ in non-uniform density clouds is proposed. This method uses the volume-averaged initial cloud density to calculate an effective density contrast ($\chi_{\rm eff}$). This modification to Jones's equation provides a better estimate of cloud disruption timescales with only a 4.59% of error.

- Our numerical convergence study quantifies that a resolution of R64 provides an optimum trade-off between computational efficiency and physical accuracy in simulating wind–cloud interactions. At this resolution, the development of RT and KH instabilities, cloud morphology evolution, and tail turbulence can be adequately tracked.

In the thesis, we have introduced a new methodology to numerically estimate the cloud-crushing time in wind-cloud interactions, considering the detailed temporal evolution of shock structures and cloud morphology. Our shock-tracking algorithm, combined with velocity-divergence and pressure-gradient maps, furnishes a powerful framework for identifying and characterizing shocks in hydrodynamical simulations. Most relevantly, this methodology lies within the purview of interstellar astrophysics, in which the dynamics of wind-cloud interaction are critical to an understanding of the lifecycle of ISM and CGM clouds and the star formation process.

Even though our study provides a good starting point toward the role of shocks in disrupting clouds, there are a number of interesting avenues for future work. Wind-cloud interaction parameter space would be better explored by increasing the space of simulated parameters to a wider range of cloud morphologies, different wind properties, and varying ambient conditions. Radiative cooling, magnetic fields, and self-gravity can still be added, increasing further the realism of our models and giving a more comprehensive picture of the general physical processes involved.

The implications of the insights obtained from our simulations reach beyond the specific calculation of the cloud crushing times. Many astrophysical parameters are defined as a function of, or, similarly to $t_{\rm cc}$, were initially derived for idealized situations. Our numerical method accounts for the dynamic evolution of shocks and cloud morphology and can be used to quantify the range of applicability of these analytical approximations to more realistic situations. It is only in incorporating these complexities of turbulent mixing, shock interactions, and the changes in morphology that we have some possibility of refining our understanding of these parameters and their implications for a wide variety of astrophysical phenomena.

Bibliography

[1] Jones, T. W.; Kang, H.; Tregillis, I. L. Cosmic Bullets as Particle Accelerators and Radio Sources. *ApJ* **1994**, *432*, 194.

[2] Klein, R. I.; McKee, C. F.; Colella, P. On the Hydrodynamic Interaction of Shock Waves with Interstellar Clouds. I. Nonradiative Shocks in Small Clouds. *ApJ* **1994**, *420*, 213.

[3] Mignone, A.; Bodo, G.; Massaglia, S.; Matsakos, T.; Tesileanu, O.; Zanni, C.; Ferrari, A. PLUTO: A Numerical Code for Computational Astrophysics. *The Astrophysical Journal Supplement Series* **2007**, *170*, 228.

[4] Mignone, A.; Zanni, C.; Tzeferacos, P.; van Straalen, B.; Colella, P.; Bodo, G. The PLUTO Code for Adaptive Mesh Computations in Astrophysical Fluid Dynamics. *ApJS* **2012**, *198*, 7.

[5] Hunter, J. D. Matplotlib: A 2D graphics environment. *Computing in Science & Engineering* **2007**, *9*, 90–95.

[6] Childs, H. *et al.* High Performance Visualization–Enabling Extreme-Scale Scientific Insight. 2012; `https://visit.llnl.gov`.

[7] Google LLC, Gemini Advance. `https://gemini.google.com`.

[8] Anand, A.; Nelson, D.; Kauffmann, G. Characterizing the abundance, properties, and kinematics of the cool circumgalactic medium of galaxies in absorption with SDSS DR16. *Monthly Notices of the Royal Astronomical Society* **2021**, *504*, 65–88.

[9] Sparre, M.; Pfrommer, C.; Vogelsberger, M. The physics of multiphase gas flows: fragmentation of a radiatively cooling gas cloud in a hot wind. *Monthly Notices of the Royal Astronomical Society* **2018**, *482*, 5401–5421.

[10] Kerber, L. O.; Libralato, M.; Souza, S. O.; Oliveira, R. A. P.; Ortolani, S.; Pérez-Villegas, A.; Barbuy, B.; Dias, B.; Bica, E.; Nardiello, D. A deep view of a fossil relic in the Galactic bulge: the Globular Cluster HP1. *Monthly Notices of the Royal Astronomical Society* **2019**, *484*, 5530–5550.

[11] López-Corredoira, M.,; Allende Prieto, C.,; Garzón, F.,; Wang, H.,; Liu, C.,; Deng, L., Disk stars in the Milky Way detected beyond 25 kpc from its center. *A&A* **2018**, *612*, L8.

[12] Draine, B. T. *Physics of the Interstellar and Intergalactic Medium*; 2011.

[13] Tumlinson, J.; Peeples, M. S.; Werk, J. K. The Circumgalactic Medium. *Annual Review of Astronomy and Astrophysics* **2017**, *55*, 389–432.

[14] Williams, A. A.; Evans, N. W. Haloes light and dark: dynamical models of the stellar halo and constraints on the mass of the Galaxy. *MNRAS* **2015**, *454*, 698–707.

[15] Tumlinson, J.; Peeples, M. S.; Werk, J. K. The Circumgalactic Medium. *Annual Review of Astronomy and Astrophysics* **2017**, *55*, 389–432.

[16] Banda-Barragán, W. E.; Parkin, E. R.; Federrath, C.; Crocker, R. M.; Bicknell, G. V. Filament formation in wind–cloud interactions – I. Spherical clouds in uniform magnetic fields. *Monthly Notices of the Royal Astronomical Society* **2015**, *455*, 1309–1333.

[17] Schneider, E. E.; Robertson, B. E. HYDRODYNAMICAL COUPLING OF MASS AND MOMENTUM IN MULTIPHASE GALACTIC WINDS. *The Astrophysical Journal* **2017**, *834*, 144.

[18] Gronke, M.; Oh, S. P. The growth and entrainment of cold gas in a hot wind. *Monthly Notices of the Royal Astronomical Society: Letters* **2018**, *480*, L111–L115.

[19] Brüggen, M.; Scannapieco, E. THE LAUNCHING OF COLD CLOUDS BY GALAXY OUTFLOWS. II. THE ROLE OF THERMAL CONDUCTION. *The Astrophysical Journal* **2016**, *822*, 31.

[20] Murray, S. D.; White, S. D. M.; Blondin, J. M.; Lin, D. N. C. Dynamical Instabilities in Two-Phase Media and the Minimum Masses of Stellar Systems. *ApJ* **1993**, *407*, 588.

[21] Xu, J.; Stone, J. M. The Hydrodynamics of Shock-Cloud Interactions in Three Dimensions. *ApJ* **1995**, *454*, 172.

[22] Miniati, F.; Jones, T. W.; Ryu, D. On the Exchange of Kinetic and Magnetic Energy between Clouds and the Interstellar Medium. *The Astrophysical Journal* **1999**, *517*, 242.

[23] Nakamura, F.; McKee, C. F.; Klein, R. I.; Fisher, R. T. On the Hydrodynamic Interaction of Shock Waves with Interstellar Clouds. II. The Effect of Smooth Cloud Boundaries on Cloud Destruction and Cloud Turbulence. *The Astrophysical Journal Supplement Series* **2006**, *164*, 477.

[24] Raga, A. C.; Esquivel, A.; Riera, A.; Velázquez, P. F. The Three-dimensional Structure of a Radiative, Cosmic Bullet Flow. *The Astrophysical Journal* **2007**, *668*, 310.

[25] Vieser, W.,; Hensler, G., The evolution of interstellar clouds in a streaming hot plasma including heat conduction. *A&A* **2007**, *472*, 141–153.

[26] Cooper, J. L.; Bicknell, G. V.; Sutherland, R. S.; Bland-Hawthorn, J. Starburst-driven galactic winds: filament formation and emission processes. *The Astrophysical Journal* **2009**, *703*, 330.

[27] Scannapieco, E.; Brüggen, M. THE LAUNCHING OF COLD CLOUDS BY GALAXY OUTFLOWS. I. HYDRODYNAMIC INTERACTIONS WITH RADIATIVE COOLING. *The Astrophysical Journal* **2015**, *805*, 158.

[28] Pittard, J. M.; Parkin, E. R. The turbulent destruction of clouds – III. Three-dimensional adiabatic shock–cloud simulations. *Monthly Notices of the Royal Astronomical Society* **2016**, *457*, 4470–4498.

[29] Banda-Barragán, W. E.; Zertuche, F. J.; Federrath, C.; García Del Valle, J.; Brüggen, M.; Wagner, A. Y. On the dynamics and survival of fractal clouds in galactic winds. *Monthly Notices of the Royal Astronomical Society* **2019**, *486*, 4526–4544.

[30] Jones, T. W.; Ryu, D.; Tregillis, I. L. The Magnetohydrodynamics of Supersonic Gas Clouds: MHD Cosmic Bullets and Wind-swept Clumps. *The Astrophysical Journal* **1996**, *473*, 365.

[31] McCourt, M.; O'Leary, R. M.; Madigan, A.-M.; Quataert, E. Magnetized gas clouds can survive acceleration by a hot wind. *Monthly Notices of the Royal Astronomical Society* **2015**, *449*, 2–7.

[32] Poludnenko, A. Y.; Frank, A.; Blackman, E. G. Hydrodynamic Interaction of Strong Shocks with Inhomogeneous Media. I. Adiabatic Case. *The Astrophysical Journal* **2002**, *576*, 832.

[33] Melioli, C.; de Gouveia Dal Pino, E. M.; Raga, A. Multidimensional hydrodynamical simulations of radiative cooling SNRs-clouds interactions: an application to starburst environments. *Astronomy &amp; Astrophysics* **2005**, *443*, 495–508.

[34] LeVeque, R. J. *Numerical Methods for Conservation Laws*; Birkhäuser Basel, 1992.

[35] LANDAU, L.; LIFSHITZ, E. In *Fluid Mechanics (Second Edition)*, second edition ed.; LANDAU, L., LIFSHITZ, E., Eds.; Pergamon, 1987; pp 313–360.

[36] Navarrete, S.; Banda-Barragán, W. A comparison of cosmological codes: properties of thermal gas and shock waves in large-scale structures. *Universidad de Investigación de Tecnología Experimental Yachay* **2011**,

[37] Teutloff, F.; Brüggen, M.; Banda-Barragán, W. Shock waves in magnetohydrodynamical simulations of galactic wind-cloud interactions. *Universität Hamburg* **2021**,

[38] Navarrete, S.; Pinargote, B. J.; Banda-Barragán, W. E. Shock waves in Interstellar Cloud-Cloud and Wind-Cloud Collisions. *Journal of Physics: Conference Series* **2024**, *2796*, 012005.

[39] Mac Low, M.-M.; McKee, C. F.; Klein, R. I.; Stone, J. M.; Norman, M. L. Shock Interactions with Magnetized Interstellar Clouds. I. Steady Shocks Hitting Nonradiative Clouds. *ApJ* **1994**, *433*, 757.

[40] Helmholtz, XLIII. On discontinuous movements of fluids. *The London, Edinburgh, and Dublin Philosophical Magazine and Journal of Science* **1868**, *36*, 337–346.

[41] HOWARD, L. N. Hydrodynamic and Hydromagnetic Stability. *Journal of Fluid Mechanics* **1961**, *13*, 158–160.

[42] Taylor, G. I. The instability of liquid surfaces when accelerated in a direction perpendicular to their planes. I. *Proceedings of the Royal Society of London. Series A. Mathematical and Physical Sciences* **1950**, *201*, 192–196.

[43] Rayleigh, Investigation of the Character of the Equilibrium of an Incompressible Heavy Fluid of Variable Density. *Proceedings of the London Mathematical Society* **1882**, *s1-14*, 170–177.

[44] Nittmann, J.; Falle, S. A. E. G.; Gaskell, P. H. The dynamical destruction of shocked gas clouds. *MNRAS* **1982**, *201*, 833–847.

[45] Goldsmith, K. J. A.; Pittard, J. M. The isothermal evolution of a shock-filament interaction. *Monthly Notices of the Royal Astronomical Society* **2019**, *491*, 4783–4801.